A new interpolation method to measure delta evolution and sediment flux: Application to the late Holocene coastal plain of the Argens River in the western Mediterranean

Jean-Philippe Degeai, Frédérique Bertoncello, Matteo Vacchi, Laurent Augustin, Alain de Moya, Luigi Ardito, Benoît Devillers

A new interpolation method to measure delta evolution and sediment flux: application to the late Holocene coastal plain of the Argens River in the western Mediterranean

Jean-Philippe DEGEAI (1)*, Frédérique BERTONCELLO (2), Matteo VACCHI (3, 4), Laurent AUGUSTIN (5), Alain DE MOYA (5), Luigi ARDITO (6), Benoît DEVILLERS (1)

(1) ASM UMR5140, Université Montpellier 3, CNRS, Ministère de la Culture, 34199 Montpellier, France
(2) CEPAM UMR7264, Université Côte d'Azur, CNRS, 06357 Nice, France
(3) Dipartimento di Scienze della Terra, University of Pisa, Via Santa Maria 53, 56126 Pisa, Italy
(4) CIRSEC, Center for Climate Change Impact, University of Pisa, Via del Borghetto 80, 56124 Pisa, Italy
(5) DT INSU, C2FN, CNRS, 83507 La Seyne sur Mer, France
(6) BRGM, Centre scientifique et technique, 45060 Orléans, France

*corresponding author
E-mail address: jean-philippe.degeai@cnrs.fr (J.-P. Degeai)

ABSTRACT

Rapid environmental changes along the Mediterranean coasts influenced the sedimentary dynamics, shoreline position and human settlements in deltaic areas over

the last millennia. An innovative and multiproxy approach using geostatistical modelling was developed to estimate geomorphic evolution and sediment fluxes in deltaic areas, while palaeoecological conditions and environmental changes were assessed from geochemistry and cluster analyses of molluscan fauna. This method was applied to the coastal plain of the Argens River (southern France) in the western Mediterranean. The study of facies associations led to the identification of depositional environments representative of prodelta, delta front, river channel, floodplain, marsh and abandoned channel. The late Holocene sediment flux in the Argens River bayhead delta ranged from 15,800 ± 2300 to 52,000 + 8500 $m^3.yr^{-1}$. The highest rates of sediment deposition and delta growth occurred between 2500 and 2000 cal yr BP during a period of high flood frequency in the western Mediterranean. A geomorphically-induced decrease in subaqueous sediment flux over the past 2500 years and an increase in fluvial activity from 1600 to 500 cal yr BP were primarily controlled by autogenic processes due to change in accommodation space, delta slope and tributary junctions. A sharp increase in subaerial sediment flux from 500 to 0 cal yr BP was probably driven by hydroclimatic change characterized by more frequent flooding during the Little Ice Age. High sediment fluxes and climate-driven fluvial activity were associated with a southward shift of the North Atlantic westerlies or a northward migration of the intertropical convergence zone.

KEYWORDS

Mediterranean delta; Coastal environment; Sediment flux; Elevation modelling; Inorganic geochemistry; Molluscan fauna; Late Holocene; Western Mediterranean

1. INTRODUCTION

In the western Mediterranean, the vulnerability of Holocene coastal landscape increased in response to rapid climate change characterized by pervasive millennial-scale variability as well as decadal- to centennial-scale abrupt transitions (Fletcher et al., 2013; Fletcher and Zielhofer, 2013; Melis et al., 2018). These rapid climate changes occurred during cooling events characterized by high storm activity and flood frequency, which led to an increased fluvial and coastal sediment supply (Dezileau et al., 2011, 2016; Sabatier et al., 2012; Fletcher and Zielhofer, 2013; Degeai et al., 2015, 2017). These episodes of intense storm activity and high flood frequency could have been caused by changes in atmospheric circulation patterns such as the North Atlantic oscillation (NAO) or the intertropical convergence zone (ITCZ) (Benito et al., 2015a, 2015b; Goudeau et al., 2015; Dezileau et al., 2016; Sanchez-Lopez et al., 2016; Degeai et al., 2017).

For instance, a southward shift of the North Atlantic westerlies and storm tracks related to the negative phase of the NAO was associated with cooler and wetter climatic conditions in southwestern Europe during the Little Ice Age (Nieto-Moreno et al., 2011, 2013a, 2013b; Trouet et al., 2012; Wirth et al., 2013; Goudeau et al., 2014, 2015; Sanchez-Lopez et al., 2016). An increase in riverine flooding and fluvial activity occurred at this time (Macklin et al., 2006; Benito et al., 2015a; Degeai et al., 2017), which led to higher inputs of terrigenous material in the marine sediments of the western Mediterranean basin (Frigola et al., 2007; Nieto-Moreno et al., 2011, 2013a, 2013b; Goudeau et al., 2014, 2015; Jalali et al., 2016).

High fluvial sediment supply to coast and river mouths led to widespread coastal plains and an increased growth of bayhead deltas in incised-valley systems (Grove, 2001; Amorosi et al., 2009; Anthony et al., 2014). However, the quantitative impact of late

Holocene climate change on the sedimentation rates and fluvial activity of western Mediterranean deltas is poorly known, although these coastal areas are important to estimate sediment transport and flux from continent to ocean, or to assess the balance between onshore erosion and offshore deposition.

The evolution of deltas developed in western Mediterranean incised-valley systems was generally characterized by facies associations showing a succession of marine, lagoonal or fluvial conditions over the past millennia (Amorosi et al., 2009, 2013b, 2013c; Bertoncello et al., 2014a; Anthony, 2015). The identification of depositional environment and the study of sedimentary processes and palaeogeographic changes in the western Mediterranean delta plains during the Holocene were generally based on multiproxy analyses of sedimentary sequences from cores or trenches (e.g. Giraudi et al., 2009; Bertoncello et al., 2014a; Amorosi et al., 2016; Melis et al., 2018; Devillers et al., 2019; Ruiz-Pérez and Carmona, 2019). These methods are effective for coastal palaeoenvironmental reconstruction, but are often poorly suited to the geometric reconstruction of sedimentary units and the measurement of sediment volumes. Geostatistics or numerical modelling were used to estimate palaeoelevation and sediment flux in coastal plains and incised-valley systems over the last millennia (e.g. Koster et al., 2017; Clement and Fuller, 2018). These interpolation methods are very useful in the case of limited age data and can provide important information on soil erosion, sediment flux, mass balance and geomorphic evolution in coastal areas.

In this paper, a new quantitative approach was developed to (1) calculate sediment flux associated with the progradation of bayhead deltas in incised-valley systems and (2) decipher the role of climate change and autogenic processes on delta growth. This new method was applied to the coastal plain of the Argens River in southeastern France, which is an area of particular interest for the study of atmospheric circulation patterns

between northern and southern Europe. The depositional environment and sedimentary dynamics over the past 2500 years were studied using an integrated methodology based on cores and archaeological excavations, sedimentological analyses (geochemistry, magnetic susceptibility), malacology and radiocarbon chronology, then geomorphic change and sediment flux were estimated from geostatistics and elevation modelling. The variability of sediment flux was discussed in relation to late Holocene hydroclimate change and geomorphic setting.

2. ENVIRONMENTAL SETTING

The Argens River drains a catchment of ca. 2800 km^2 located in southeastern France (Fig. 1A). This 114 km long river flows into the western Mediterranean between the Gulf of Lions and the Ligurian Sea along the southwestern Alps. This mountainous coastal area is bordered by a very narrow shelf (< 5 km) and a steep continental slope that stands above the floor of the Provençal Basin at depths greater than 2800 m. The source of the Argens River is at 268 m above sea level (Durozoy et al., 1970), giving an average slope of ca. 2.35‰ for the modern streambed. Over the last 50 years (1970-2019), the hydrological regime at Roquebrune-sur-Argens (Fig. 1B) was characterized by maximum and minimum river discharge rates in winter (32.2 $m^3.s^{-1}$) and summer (5.8 $m^3.s^{-1}$), respectively, due to a Mediterranean rainfall regime (DREAL PACA data, www.hydro.eaufrance.fr).

The lower valley of the Argens River is bounded on the south by the late Proterozoic to early Carboniferous granitic and gneissic rocks of the Massif des Maures (Fig. 1B), and on the north by the Permian volcano-sedimentary basin of the lower Argens valley (Toutin-Morin et al., 1994). At the end of the Last Glacial Maximum (LGM, ca. 20 cal kyr

126 BP), sea level dropped more than 100 m along the French Mediterranean coast
127 (Lambeck and Bard, 2000), leading to an adjustment of the longitudinal profile of the
128 river by regressive erosion (Bertoncello et al., 2014a). Thus, the lower valley of the
129 Argens River was deeply incised in Lower Pliocene marine sediments composed of
130 blueish or grey marl, sand and gravel (Toutin-Morin et al., 1994). This incised-valley
131 system was then buried by transgressive deposits during the post-LGM sea level rise
132 (Dubar, 2004).
133 In the lower valley, the post-LGM deposits form a >100 m thick sedimentary sequence
134 composed of (1) fluvial sand and gravel at the bottom, (2) marine sand and clay
135 intercalated with fluvial sand and gravel, and (3) fluvial silt, sand and gravel at the top
136 (Durozoy et al., 1970; Toutin-Morin et al., 1994; Dubar, 2004). The latter deposits were
137 formed by delta progradation and fluvial aggradation, which led to the formation of a
138 coastal plain over the past 4000 years (Dubar, 2004; Bertoncello et al., 2014a). This
139 coastal plain does not exceed 5 m in elevation over a distance of up to 5 km from the sea
140 (Fig. 1B), giving a mean slope of 1‰.
141 Previous works studied the palaeogeographic and environmental changes in the Argens
142 River coastal plain from the Neolithic to the Roman period and their impacts on human
143 settlement (Dubar, 2004; Bertoncello et al. 2014a). The analyses of the palaeogeography
144 at the mouth of the Argens River over the past three centuries from historical maps or
145 archives highlighted a highly mobile coastal environment under the influence of the
146 progradation of the Argens River along with its two main northern tributaries (i.e. the
147 Garonne and Reyran rivers) and the southern branch of this delta system upstream from
148 the Villepey Pond (Fig. 1B) (Cohen, 1997; Bertoncello et al., 2008, 2014a). In fact, these
149 multiple channels formed a deltaic plain, hereafter called the Argens River delta system
150 (ARDS).

151 The ARDS was classified as a bayhead delta that prograded into a protected bedrock
152 embayment with low incident wave energy as a result of significant refraction,
153 diffraction and nearshore dissipation (Anthony et al., 2014; Anthony, 2015). Bayhead
154 deltas prograde in river-mouth setting along the inner part of wave-dominated estuaries
155 (Dalrymple et al., 1992; Amorosi et al., 2005; Anthony et al., 2014), and become
156 increasingly shaped by waves (Anthony, 2015). In the western Mediterranean, wave-
157 dominated estuaries were filled with sediments during transgression then transformed
158 into wave-dominated deltas during sea-level highstand (Amorosi and Milli, 2001; Milli et
159 al., 2013). Confined or unconfined bayhead deltas are defined according to the geological
160 and environmental setting: the former prograde into incised-valleys and their geometry
161 is controlled by the morphology of the valley, while the latter prograde into open
162 interdistributary bay and are a part of larger deltaic complexes (Simms and Rodriguez,
163 2015; Simms et al., 2018). The ARDS bayhead delta is confined in the Argens River valley
164 west of Fréjus, and unconfined in the interdistributary bay between Saint-Raphaël and
165 Saint-Aygulf (Fig. 1B).
166 During the Late Holocene, or the Meghalayan (i.e. the last 4200 years b2k),
167 palaeoenvironmental and palaeoecological studies showed that the progradation of the
168 ARDS occurred in a marine depositional environment that gradually transformed into a
169 delta plain during the late phases of sedimentary filling of the lower valley (Allinne et al.,
170 2006; Devillers and Bonnet, 2006; Bertoncello et al., 2014a). Pollen data indicate that
171 the first human impact on the landscape of the lower valley of the Argens River could
172 have occurred around 7000 cal yr BP with indices of forest clearing and evidence of
173 cereal cultivation during the late Neolithic period (Dubar et al., 2004; Bertoncello et al.,
174 2014a). After ca. 3000 cal yr BP, human activities led to radical changes in the vegetation

cover, high forest clearing and metal pollution in the sediments of the ARDS (Dubar et al., 2004; Bertoncello et al., 2014a; Véron et al., 2018).

The past human occupation in the study area was more intense during the Roman period, especially from the creation of the Roman colony of *Forum Iulii* (Fréjus) (Fig. 1B) in the late first century BCE (Gascou, 1982; Gascou and Janon, 1985). The Roman harbour of *Forum Iulii* is now more than 1 km inland from the sea owing to the progradation of the ARDS during the last two thousand years (Excoffon et al., 2006, 2010; Gébara and Morhange, 2010; Bertoncello et al., 2011; Bony et al., 2011; Giaime et al., 2019).

3. MATERIAL AND METHODS

3.1. Cores and trenches

A geological database was created from sedimentary cores and archaeological trenches (Fig. 1B). It is based on published cores with geochronological and palaeoenvironmental data as well as on two new cores (BN1 and BN5) located in the downstream part of the ARDS. The 12-m long BN1 core (43°25'22''N, 6°44'02''E, 1.65 m in elevation) was sampled with a stationary piston corer. The 18.5-m long BN5 core (43°25'02''N, 6°43'44''E, 1.67 m in elevation) was sampled with a stationary piston corer from 0 to 3 m depth, a solid tube sampler equipped with a hydraulic hammer from 3 to 7 m depth, and a rotary drill auger from 7 to 18.5 m depth. The sediments at 3-4 m depth in the BN1 core and at 3.4-4 and 5.63-6.75 m depth in the BN5 core were unsampled due to creeping and difficulty in coring layers with very coarse particles.

3.2. Molluscan analysis

A volume of sediment of ca. 1000 cm^3 per sample was collected at an average interval of 50 cm along the BN1 and BN5 cores for a malacological study. These samples were sieved using a 1 mm mesh (Sabatier et al., 2008, 2012; Dezileau et al., 2016). A total of 2314 mollusc shells were identified and counted under stereomicroscope, representing 85 species living in marine (44 species), brackish (7 species), freshwater (17 species) or terrestrial (17 species) environments. The mollusc species were assigned to ecological groups from previous work in the Argens River valley (Devillers and Bonnet, 2006) and from the World Register of Marine Species (www.marinespecies.org), the AnimalBase of the University of Göttingen (www.animalbase.uni-goettingen.de) and the INPN database of the Museum National d'Histoire Naturelle (inpn.mnhn.fr).

3.3. Geochemistry

Geochemical analyses of sediments may provide information about the degree of salinity in subaqueous depositional environment from coastal or lacustrine areas: high (low) values of S, Cl and Sr can evidence brackish (freshwater) conditions (Lopez-Buendia et al., 1999; Chagué-Goff et al., 2002; Schofield et al., 2010; Moreno et al., 2012; Haenssler et al., 2013; Degeai et al. 2015, 2017). Moreover, the bulk of sulphur in coastal lakes can reflect the organic content of a sediment as a function of primary productivity in the water column (Striewski et al., 2009; Haenssler et al., 2013). High ratios of S/Cl may indicate organic-rich layers as S is high in organic-rich sediments (Croudace et al., 2006). Besides, an increase in Si, K and Rb is generally associated with riverine input in the western Mediterranean (Frigola et al., 2007; Martin-Puertas et al., 2010, 2011; Nieto-Moreno et al., 2011, 2013a; Rodrigo-Gamiz et al., 2011, 2014; Moreno et al., 2012; Martinez-Ruiz et al., 2015; Degeai et al., 2017). Elemental concentrations of coastal sediments from the western Mediterranean are usually normalized to Al to minimize

matrix effects (Dezileau et al., 2011, 2016; Sabatier et al., 2012). Therefore, we have used the Cl/Al and Sr/Al ratios as paleosalinity indicators, the Si/Al, K/Al and Rb/Al ratios as proxy records of riverine input, and the S/Cl ratio as an indicator of organic matter content.

A total of 108 and 138 sediment samples from the BN1 and BN5 cores, respectively, were measured by energy-dispersive X-ray fluorescence (ED-XRF) spectrometry at an average sampling interval of ca. 10 cm with a Delta Innov-X spectrometer equipped with a 4 W Au-tube. Each sample was dried then mechanically crushed and homogenized to a fine powder, which was placed in a crystal polystyrene tube of 22 mm length and inner diameter then covered with an ultrafine polyethylene film. The measurement of S, Cl, Rb and Sr was undertaken with the soil analytical mode, while Al, Si and K were measured with the mining analytical mode. The parameters of voltage, amperage and counting times were as follows: 10 kV, 200 μA and 10 s for Al, Si and K; 15 kV, 200 μA and 45 s for S and Cl; 40 kV, 100 μA and 30 s for Rb and Sr. The elemental concentrations were obtained using the Compton Normalization calibration method (EPA, 2007). The 2-σ measurement uncertainty is lower than ± 5% for Si, K, Rb and Sr, and around ± 10% for S and Cl.

3.4. Magnetic susceptibility

In deltaic environment, the magnetic susceptibility can reflect the terrigenous flux derived from fluvial processes (Delile et al., 2015). Higher values of magnetic susceptibility are generally driven by the presence of Fe-bearing minerals (e.g. biotite) in the sample (Dearing, 1999).

The mass-specific magnetic susceptibility (χ) of sediments from the BN1 and BN5 cores was measured at an average sampling interval of ca. 10 cm with a Bartington MS2

susceptibilimeter and a MS2B probe. Each powder sample in the tubes used for geochemical analyses (i.e. 246 samples for BN1 and BN5) was weighed then measured twice with a time period of 12s, an operating frequency of 4.65 kHz, an amplitude of applied magnetic field of 250 μT, and a resolution of $1x10^{-8}$ $kg.m^{-3}$ (range 0.1). The relative standard deviation of both measurements is systematically lower than 3%.

3.5. Geochronology

The geochronological data are based on a compilation of available radiocarbon ages in the ARDS, including a set of 10 new Accelerator Mass Spectrometry (AMS) ^{14}C dates on wood and charcoal from the BN1 and BN5 cores (Table 1). The new AMS ^{14}C ages were performed by the Centre de Datation par le RadioCarbone at Lyon and by the Poznan Radiocarbon Laboratory. The Calib 7.10 software (Stuiver et al., 2019) was used to calibrate the new ^{14}C dates and to update the calibration of radiocarbon ages published in previous studies. The radiocarbon ages of terrestrial material (seed, wood, charcoal, peat) were calibrated using the IntCal13 calibration curve (Reimer et al., 2013), while the radiocarbon ages of marine shell were calibrated using the MARINE13 calibration curve (Reimer et al., 2013) and a ΔR of -15 years (Siani et al., 2000). The 2-σ uncertainty interval and median probability of calibrated ages are reported in Table 1.

3.6. Geostatistics

Three 2D age-elevation transects (A1-3, see location in Fig. 1B) and five maps of sediment thickness in the ARDS were computed for the last 2500 years using the ArcGIS 10 Geostatistical Analyst extension. The geochronological and sediment thickness data were interpolated using radial basis functions. The computation of rasters of sediment thickness with a spatial cell of 15 m in size for each 500-year interval over the past 2500

275 years was based on the isochrones of the 2D age-elevation models and on a null
276 thickness assigned to the boundary of Holocene deposits. The models were limited to
277 the last 2500 years because there are not enough ^{14}C dates without age reversals to
278 make a robust data interpolation before 2500 cal yr BP (Table 1).
279 The palaeoelevation Z_n was then calculated at a 500-year interval from n = 1 (500 cal yr
280 BP) to 5 (2500 cal yr BP) using the ArcGIS 10 raster calculator and equation [1]. For
281 spatial coordinates (x, y), Z_n was obtained by substracting the cumulative sediment
282 thickness T from the modern elevation Z_0, which is deduced from LiDAR data available
283 for the ARDS (Litto3D, IGN/SHOM, year 2015), and by adding the sea level S_n at the time
284 n from Vacchi et al. (2016).
285
286 $$Z_n(x, y) = Z_0(x, y) - \sum_{i=1}^{n} T_i(x, y) + S_n \quad [1]$$
287
288 Error estimates for sediment thickness and palaeoelevation were calculated with an
289 uncertainty of ± 100 years for the isochrones of the 2D age-elevation models. This 200-
290 year interval was chosen because it closely matches the mean 2-σ uncertainty interval
291 (225 years) of calibrated radiocarbon ages (Table 1).
292
293
294 4. RESULTS
295 4.1. Lithology
296 Both BN1 and BN5 cores were divided into 4 stratigraphic units from bottom (unit 1) to
297 top (unit 4) (Fig. 2, 3).
298 Unit 1 in BN1 core (12-9 m depth) is characterized by alternating 10-20 cm thick layers
299 of grey to greyish brown clay, silt and fine sand (Fig. 2). Moreover, particulate organic

matter is abundantly present in the matrix of sediments deposited from 11.8 to 10.2 m depth. In BN5 core, unit 1 (18.5-11.4 m depth) is primarily composed of grey clay and silty clay alternating with grey clayey silty fine sand at ca. 16 and 14.1-13.4 m depth, with brownish grey sand at ca. 18.4, 17.5, 16.8 and 16.4 m depth, and with grey sand and gravel at 16.5 and 12.7-12 m depth (Fig. 3). The clay content decreases above 14.85 m depth.

Unit 2 in BN1 core (9-4 m depth) is mainly composed of grey, greyish brown, brownish grey or brown sand interbedded with silt and sandy silt (Fig. 2). The upper part shows a coarsening-upward trend from silt to medium-coarse sand. Thin organic-rich layers can be observed at 8.7-8.6, 8.25-8, 6.3-6.1 and 5.3-5.2 m depth, while charcoals are present around 5.7 m depth. In BN5 core, unit 2 (11.4-6.75 m depth) exhibits a succession of grey sediments characterized by a general coarsening-upward trend showing fine sandy silt and silty fine sand overlaid with fine sand from 8.5 to 8.1 m depth then with clayey medium-coarse sand and rounded gravel from 8.1 to 7.3 m depth. Particulate organic matter appears at ca. 11.3-11.2, 9.6-9.4 and 8.7-8.5 m depth (Fig. 3). The top of unit 2 in BN5 core is composed of organic-rich grey clay between 7.3 and 6.75 m depth with black peat from ca. 7 to 7.2 m depth. This layer is absent in BN1.

Unit 3 in BN1 core (3-1.4 m depth) is represented by brown sand and clast-supported rounded gravel showing a general upward-fining trend with fine-medium sand overlying coarse sand and gravel (Fig. 2). In BN5 core, the coarse sand and clast-supported rounded gravel of unit 3 (5.63-4 and 3.4-2.9 m depth) have a brownish grey or greyish brown colour in the lower part and a brown colour above 4.85 m depth (Fig. 3). The bottom of this unit is uncertain in BN5 core given the coring gap from 6.75 to 5.63 m depth.

Unit 4 in BN1 core (1.4-0 m depth) is composed of brown clay, silt and fine sand with many rootlets and of a 20 cm thick dark brown clayey layer at the bottom (Fig. 2). In BN5, unit 4 (2.9-0 m depth) is mainly composed of brownish grey or greyish brown fine sand interbedded with thin layers of clay and silty clay between 2.9 and 2.2 m depth, of greyish brown clay between 2.2 and 1.5 m depth, and of brown silt, clayey silt or fine sand between 1.5 and 0 m depth (Fig. 3). Small fragments of modern ceramics and a 15 cm thick layer of dark brown silt and matrix-supported angular or rounded gravel overlaid with a 4 cm thick layer of black organic silt appear in the upper 40 cm of BN5 core. Unit 4 in BN5 core contains particulate organic matter, rootlets and charcoals. Overall, bedding contacts are gradual apart from sand layers which are generally in sharp contact with clay or silt beds. Marine, brackish, freshwater gastropods and bivalves are present in units 1 and 2, while terrestrial gastropods are over-represented in unit 4. Unit 3 is barren of fossils.

4.2. Molluscan shells

The palaeoecological conditions prevailing in the BN1 and BN5 cores were deduced from a multivariate cluster analysis of molluscan assemblages (Fig. 4, 5).

Unit 1 is characterized by a salinity-stressed marine environment with low to moderate brackish and freshwater influences. The dominant species of this ecosystem correspond to *Turbonilla lactea* for BN1 (41% on average) and to *Moerella donacina* for BN5 (19% on average). Subordinate marine species (1-10% on average) are represented by *Abra prismatica*, *Corbula gibba*, *Eulima bivittata*, *Macomangulus tenuis*, *Smaragdia viridis*, *Thracia pubescens*, *Trivia arctica* and *Trophonopsis muricata* for BN1, and by *A. prismatica*, *Acanthocardia* sp., *Antalis dentalis*, *C. gibba*, *Gouldia minima*, *Lentidium mediterraneum*, *M. tenuis*, *Mathilda quadricarinata*, *Megastomia conoidea*, *Mimachlamys*

varia, *Nucula nucleus*, *Saccella commutata* and *Venus verrucosa* for BN5. A low to moderate mean abundance (1-12% in BN1 or BN5) of molluscs such as *Abra alba*, *Cerastoderma glaucum*, *Hydrobia acuta*, *Loripes orbiculatus*, *Parvicardium exiguum*, *Ancylus fluviatilis*, *Bithynia tentaculata*, *Islamia spirata* and *Valvata* sp. suggests that the marine environment experienced brackish and freshwater conditions with fluvial discharges.

Unit 2 is characterized by brackish and freshwater environmental conditions with marine influences (Fig. 4, 5). The molluscan assemblages are predominantly composed of *A. Alba*, *C. glaucum*, *H. acuta* and *Valvata* sp. (> 10% on average in BN1 or BN5). Other subordinate brackish or freshwater species in BN1 or BN5 include *A. fluviatilis*, *Belgrandia gibba*, *B. tentaculata*, *Euglesa casertana*, *I. spirata* and *Theodoxus fluviatilis* (1-10% on average). The rare occurrence (< 1%) of terrestrial molluscs usually found in sandy dunes such as *Cernuella virgata*, *Cochlicella conoidea*, *Trochoidea trochoides* and *Xerosecta explanata* suggests reworking of coastal sediment, while a low to moderate mean abundance (1-12% in BN1 or BN5) of *Abra nitida*, *A. prismatica*, *C. gibba*, *L. mediterraneum*, *Lucinella divaricata*, *M. donacina*, *N. nucleus*, *Retusa umbilicata*, and *T. lactea* highlight marine influences.

Unit 3 is barren of molluscan shells, whereas unit 4 is characterized by a terrestrial environment with low to moderate humid conditions (Fig. 4, 5). The most abundant land snails are represented in BN1 and BN5 by species living in dry habitats of coastal areas like sandy dunes or beaches: *C. virgata* (45 and 30% on average, respectively) and *C. conoidea* (7 and 43% on average, respectively). The most frequent subordinate terrestrial species (1-10% on average) correspond to gastropods living in dry vegetation or on sandy dunes in coastal areas (*Cochlicella acuta*, *Trochoidea pyramidata*, *T. trochoides*, *X. explanata*). Other uncommon land molluscs (< 6% on average) live in

374 either humid habitats (*Cecilioides acicula*, *Oxychilus draparnaudi*, *Oxyloma elegans*,
375 *Vallonia pulchella*) or open habitats with very variable humidity (*Vertigo pygmaea*). The
376 main species of freshwater molluscs are *B. tentaculata*, *Galba truncatula*, *I. spirata*,
377 *Musculium lacustre* and *Valvata* sp. (1-10% on average). A rare occurrence (< 3%) of *H.*
378 *acuta* is found between 1.5 and 1 m depth in BN1, while the absence of marine shells is
379 observed in both BN1 and BN5 cores.
380
381 4.3. Geochemical data
382 Unit 1 generally exhibits high values of Cl/Al and Sr/Al, which reflect high levels of
383 salinity (Fig. 2, 3). However, higher than average riverine inputs (K/Al and Rb/Al but not
384 Si/Al) accompanied with lower values of Cl/Al and Sr/Al at the bottom of BN1 and BN5
385 cores could reveal fluvial influence in a marine depositional environment. The layers of
386 brownish grey sand or grey sand and gravel in unit 1 of BN5 are associated with peaks
387 of Si along with low levels of salinity (Fig. 3). These coarse sediments could reflect local
388 and brief episodes of high-energy fluvial input. The high content of S at the transition
389 between units 1 and 2 from 9.3 to 8.1 m depth in BN1 is associated with abundant
390 tabular crystals of euhedral gypsum in the sand fraction (Fig. 2).
391 Unit 2 is characterized by a general decrease of salinity indicators paralleled by an
392 increase in riverine input indicators (Fig. 2, 3). The values of elemental ratios in the
393 upper part of unit 2 show low levels of salinity and high riverine input in both BN1 and
394 BN5 cores. In this latter, the organic-rich clayey layer at the top of unit 2 exhibits high
395 ratios of K/Al, Rb/Al and S/Cl, while the highest concentration of S is found in the black
396 peat horizon between ca. 7.2 to 7 m depth.

Unit 3 presents geochemical and sedimentological features characterized by high Si/Al and K/Al ratios, low salinity indices, and coarse sand and gravel most likely deposited in high-energy environment (Fig. 2, 3).

Unit 4 in BN1 core shows higher than average riverine discharge and very low levels of salinity (Fig. 2). Large peaks of K/Al and Rb/Al are associated with a 20 cm thick layer of dark brown clayey sediment at the bottom of this unit. Besides, a major peak of S/Cl is found at the transition between units 3 and 4 in BN1 core, and is perhaps indicative of higher organic matter content. In BN5 core, the lower half of unit 4 between 2.9 and 1.55 m depth generally shows higher than average Rb/Al and K/Al ratios, low Si/Al ratio, and peaks of Sr/Al, whereas lower than average indicators of riverine input and salinity are most often found in the upper half of this unit above 1.55 m depth (Fig. 3).

Overall, high (low) levels of salinity in both BN1 and BN5 cores generally correspond to low (high) levels of riverine input. Hence, the variability of salinity indicators in the ARDS could have been mainly driven by fluvial activity. Besides, the geochemical indicators of riverine discharge seem to have been influenced by the grain size of sediments. High values of Si/Al are found only in sand and gravel, and more specifically in the coarse sand and gravel fraction (Fig. 2, 3). High values of Rb/Al are observed only in clay and silt, while high values of K/Al can be recorded in coarse or fine sediments. K and Rb are commonly associated with detrital clay (Croudace et al., 2006). However, the K/Al ratio is also influenced by the contribution of detrital K-feldspar, which may be significant in the coarse fraction (Martinez Ruiz et al., 2015).

4.4. Magnetic susceptibility

The values of mass-specific magnetic susceptibility (χ) are generally lower than $10x10^{-8}$ $m^{-3}.kg^{-1}$ in BN1 and BN5 (Fig. 2, 3). Higher than average χ values are found in the basal

part of both cores (unit 1) from 12 to ca. 10 m depth in BN1 and from 18.5 to 16.9 m depth in BN5. χ values ranging between ca. 10 and 20x10^{-8} $m^{-3}.kg^{-1}$ appear from 5.8 to 4.5 m depth in unit 2 of BN1 and from 3.3 to 2 m depth at the transition between units 3 and 4 in BN5. The highest χ values around 30x10^{-8} $m^{-3}.kg^{-1}$ are found at the top of BN1 and BN5 cores.

Higher χ values in deltaic environment should reflect a terrigenous supply from catchment by fluvial processes (Delile et al., 2015). However, the riverine sediments of unit 3 are characterized by low χ values (Fig. 2, 3). In fact, the mineralogical composition of coarse sand and gravel can preclude the use of magnetic susceptibility as a reliable proxy record of fluvial activity. The low χ values of sediments from unit 3 suggest that these coarse alluvial deposits are mainly composed of diamagnetic material such as quartz (Dearing, 1999). High values of Si and Si/Al as in unit 3 can be indicative of high relative content of quartz (Martinez-Ruiz et al., 2015). This is confirmed by stereomicroscopic observations, which show that the alluvial deposits of unit 3 exhibit an important content of quartz for particles coarser than 1 mm.

By contrast, the high χ values of the fine sediments in the upper 1.5 m of BN5 are not related to high values of elemental ratios indicative of riverine input. In fact, this increase in magnetic susceptibility could have been caused by post-depositional oxidation and weathering of sediments at the top of the BN5 core, which is characterized by a terrestrial environment as evidenced by molluscan fauna (Fig. 3, 5).

5. PALAEOENVIRONMENTAL INTERPRETATION

Delta systems in the northwestern Mediterranean are often characterized by a vertical stacking of mid-late Holocene prodelta, delta front and delta plain deposits (Dubar and

447 Anthony, 1995; Amorosi et al., 2008, 2013c). These deltaic sequences are interpreted as
448 highstand systems tracts deposited during the deceleration of sea level rise after 7500
449 cal yr BP (Stanley and Warne, 1994; Somoza et al., 1997; Vacchi et al., 2016).
450 The depositional environments of the BN1 and BN5 sedimentary successions can be
451 defined on the basis of a comparison of molluscan assemblages, lithology, sediment
452 properties and geochemical data (Fig. 2-5) with facies associations described for the
453 northwestern Mediterranean deltas of (1) the Argens River (Allinne et al., 2006;
454 Devillers and Bonnet, 2006; Bertoncello et al., 2014a), Hérault River (Devillers et al.,
455 2019), Rhône River (Amorosi et al., 2013c) and Var River (Dubar and Anthony, 1995) in
456 southern France, (2) the Arno River (Amorosi et al., 2009, 2013a, 2013b), Biferno River
457 (Amorosi et al., 2016), Po River (Amorosi et al., 2008), Posada River (Melis et al., 2018)
458 and Tiber River (Giraudi et al., 2009) in Italy, and (3) the Ebro River (Somoza et al.,
459 1997) and Turia River (Ruiz-Pérez and Carmona, 2019) in eastern Spain (Fig. 1A).
460 Holocene prodeltas in the northwestern Mediterranean are characterized by (1)
461 salinity-stressed and strongly fluvial-influenced marine environment with abundant
462 marine gastropods and mixed brackish-normal saline conditions, and (2) clay-sand
463 alternations showing an upward decrease in clay content accompanied with an increase
464 in the frequency and thickness of sandy layers (Somoza et al., 1997; Amorosi et al., 2008,
465 2009, 2013b, 2013c). In both BN1 and BN5 cores, unit 1 is mostly composed of grey to
466 brownish grey clay and silty clay with intercalations of sand layers deposited in a
467 marine environment with high levels of salinity (Fig. 2, 3). From the bottom to the top of
468 unit 1, the sandy layers are thicker or more frequent and clay content decreases. In BN5
469 core, the presence of massive mud below 17 m depth and the increasing sand content
470 above this depth fit well with the bottom sediment distribution of the modern inner
471 shelf environment along the ARDS, which shows a minimum upper limit of onshore

blue-grey mud and a minimum lower limit of nearshore terrigenous sand at ca. 15 m below sea level (Toutin-Morin et al., 1994). The abundance of marine molluscs ranges from ca. 45 to 75% in BN1 core and from ca. 50 to 95% in BN5 core. Moreover, riverine inputs highlight a marine environment with fluvial influence. Hence, unit 1 is defined as a prodelta.

In the northwestern Mediterranean, the sedimentary features associated with the transition from prodelta to delta front typically exhibits an increasing proportion of sand, with a delta front composed of an upward-coarsening sand body deposited in high-energy environment (Somoza et al., 1997; Amorosi et al., 2008, 2013c). The lower and middle parts of unit 2 in BN1 and BN5 cores are characterized by many layers of sandy silt or fine sand, while the upper part shows upward-coarsening sand bodies in which the sand fraction changes from fine sand to medium-coarse sand from bottom to top (Fig. 2, 3). Unit 2 is also characterized by a decrease in marine shells (from ca. 50 to 0%) paralleled by a decrease in Cl/Al and an increase of riverine input (Fig. 2, 3). This unit can be considered as a ca. 5 m thick delta front, which is consistent with the delta front thickness of 5.5 and 7 m in PL1 and PAL1 cores, respectively (Fig. 6). In BN5 core, the delta front is overlaid with organic-rich sediments and black peat, which were likely deposited in a marsh environment (Fig. 3).

The sediments of unit 3 are composed of poorly sorted coarse sand and clast-supported gravel devoid of fossils (Fig. 2, 3). Fining-upward trends are found in unit 3 at BN1 and from the top of unit 3 to the lower half of unit 4 at BN5. These sedimentological and biological features are typical of high-energy environments such as fluvial channels (Dubar and Anthony, 1995; Somoza et al., 1997; Amorosi et al., 2009, 2013a, 2013b, 2013c, 2016; Giraudi et al., 2009; Melis et al., 2018; Devillers et al., 2019; Ruiz-Pérez and Carmona, 2019). Moreover, a deposition of the coarse sediments of unit 3 in a river

channel is consistent with the geochemical data, which show very low levels of salinity and high values of Si/Al and K/Al indicative of riverine input.

Unit 4 in BN1 core and the upper half of unit 4 in BN5 core are mainly composed of bioturbated brown clay, silt and fine sand with land molluscs and very low levels of salinity (Fig. 2, 3). These sedimentological and palaeoecological features are compatible with a depositional environment in a well-drained floodplain occasionally affected by river floods (Somoza et al., 1997; Allinne et al., 2006; Devillers and Bonnet, 2006; Amorosi et al., 2013a, 2016; Bertoncello et al., 2014a; Melis et al., 2018; Devillers et al., 2019; Ruiz-Pérez and Carmona, 2019). The delta plain of the ARDS includes both floodplain and river channels. More specifically, the malacological data point to a delta plain environment subject to subaerial exposure, given the high abundance of terrestrial species living in coastal habitats such as *Cernuella virgata*, *Cochlicella conoidea*, *Trochoidea trochoides* and *Xerosecta explanata* at the top of BN1 and BN5 cores (Fig. 4, 5). Land snails and freshwater molluscs associated with humid or aquatic environment are mostly found in the lower part of unit 4 and are probably indicative of a depositional setting more frequently subjected to riverine flooding or hydromorphic conditions.

In the lower half of unit 4 in BN5 core, thin layers of brownish grey to greyish brown sand and silt (ca. 2.9-2.2 m depth) then organic-rich greyish brown massive clay with rootlets at the top (ca. 2.2-1.5 m depth) were deposited on the coarse fluvial sediments of unit 3 (Fig. 3). These sediment properties and the stratigraphic relationship with fluvial-channel sediments are typical of alluvial sub-environments close to river channel (Amorosi et al., 2013a, 2016). Besides, the organic-rich sediments of the lower half of unit 4 in BN5 core show a general fining-upward trend such as in abandoned channel fills, which are characterized by an initial proximal fill during the abandonment stage then by a distal fill collected in the abandoned palaeochannel during the disconnected

522 stage (Toonen et al., 2012). These two stages of channel-fill development could explain
523 the sediment deposition at ca. 2.9-2.2 and 2.2-1.5 m depth, respectively, in BN5 core.
524 Higher than average values of Sr and Sr/Al are recorded in the lower half of unit 4 in
525 BN5 core and could be due to episodes of shallowing and salinization of water bodies in
526 an abandoned fluvial channel, for example during hydroclimatic changes. Indeed,
527 enhanced Sr may indicate the presence of high-Sr aragonite which requires a shallow-
528 water source (Croudace et al., 2006). Besides, higher Sr/Al ratios were recorded by
529 Holocene lacustrine deposits in the western Mediterranean during periods of evaporite
530 precipitation due to lower lake levels characterized by Sr-rich sediments (Martin-
531 Puertas et al., 2011).
532
533
534 6. NUMERICAL MODELLING
535 6.1. 2D age-elevation models
536 An accurate chronology of deltaic sequences can be difficult to determine because of ^{14}C
537 age reversals due to sediment storage and remobilization of older deposits during
538 downslope alluvial transport that prevails in fluvial and delta plains (Stanley and Hait,
539 2000; Stanley, 2001).
540 The median probability of 10 new radiocarbon dates obtained for the BN1 and BN5
541 cores ranges from 3565 to 440 cal yr BP (Table 1). However, the 4 radiocarbon ages of
542 charcoals and wood sampled in delta front deposits are too old and show a reversal of
543 the median probability (Fig. 2, 3). This seems to indicate that reworking of older
544 terrestrial organic matter from the catchment was more important in the delta front
545 depositional environment. By excluding these 4 radiocarbon ages, the sediments from

546 the BN1 and BN5 cores would have been deposited approximately during the last 2500
547 years.
548 Amongst the 41 radiocarbon dates compiled in the ARDS, we discarded 12 dates (ca.
549 30% of total) showing age reversals with a median probability older than expected
550 (Table 1). These reversal patterns are probably due to the remobilization and
551 redeposition of older material (Stanley and Hait, 2000; Stanley, 2001). The cores from
552 the ancient harbour of *Forum Iulii* (FIX, FXI, SC6) (Fig. 1B) were not used owing to
553 potential sedimentary hiatuses caused by possible dredging in this port basin during the
554 Roman period (Bony et al., 2011). Besides, several ^{14}C dates from the PL1 core exhibit
555 large 2-σ uncertainty intervals higher than 300 years because of a very large plateau of
556 the calibration curve from ca. 800 to 400 cal yr BCE (i.e. a conventional ^{14}C age around
557 2450 BP), the so-called Hallstatt plateau (Fontugne, 2004; Van der Plicht, 2004). Finally,
558 a total of 29 radiocarbon ages were used to compute three 2D age-elevation models in
559 the ARDS: one longitudinal age profile (A1) and two transverse age profiles (A2 and A3)
560 across the valley (Fig. 6). The isochrones are displayed with a 100-year resolution.
561 Overall, profile A1 shows a downstream thickening of deposits from PL1 to BN5 over the
562 last 2500 years. The thickest part is located between PAL1 and BN5 where a mean
563 sediment thickness of ca. 18 m was deposited during the last 2500 years. The highest
564 accumulation occurred between 2500 and 2000 cal yr BP in this part of profile A1.
565 Profile A2 and the northwestern part of profile A1 exhibit a lower sediment
566 accumulation with a thickness of ca. 5 m upstream of the ARDS during the last 2500
567 years. Profile A3 shows that the sediments deposited downstream of the coastal plain
568 over the past 2500 years are thicker in the central part of the valley around BN5 and
569 thinner on the southern edge of the ARDS, with a thickness of ca. 7 m in the VIL2 core
570 (Fig. 6). On the northern side, the trench dug during the Théâtre d'agglomération T2

(TAT2) archaeological excavation revealed that Permian rocks were buried under coastal sediments during the second half of the first century BCE (Excoffon et al., 2006; Devillers et al., 2007). These Permian rocks were then covered by 2-3 m of sediments over the last 2000 years.

Although the lack of chronological data in the easternmost part of the ARDS coastal plain does not allow the age models to be robustly estimated in this area, LiDAR data were shifted along the BN5 age-elevation model in order to propose a hypothetical reconstruction of the isochrones of the unconfined bayhead delta that prograded onto the inner shelf (Fig. 6). The depositional architecture and stacking pattern east of BN5 are thus very similar to those of steep-face deltas studied by Dubar and Anthony (1995) along the southern French Alps, such as the Var River delta located at ca. 70 km northeast of the Argens River (Fig. 1A).

6.2. Sediment thickness

The numerical models of sediment thickness of the Argens River bayhead delta cover an area of 12.2 km^2 (Fig. 7). These spatial models were focused on the incised-valley system west of Fréjus, in which the eastward progradation of the bayhead delta of the Argens River was confined and controlled by the morphology of the valley. Moreover, the lack of data in the easternmost part of the ARDS coastal plain prevents the models to be extended east of Fréjus. Therefore, the eastern limit of the modelled area corresponds approximately to the eastern boundary of the Argens River valley between Fréjus and the eastern side of the Massif des Maures.

The thickness of sediments deposited from 2500 to 2000 cal yr BP ranges from < 1 to 8 m in the study area, with maximum values around the PAL1 site (Fig. 7A). The depocenter was located in the central part of the lower valley of the Argens River. From

2000 to 1500 cal yr BP, the depocenter moved downstream in an eastward direction (Fig. 7B). The main depositional area was located between BN5 and BN1, with a maximal thickness of deposits estimated between 4 and 5 m. Another area of moderate accumulation ranging from 1 to 3 m in thickness can be observed along a northwest-southeast direction of the valley from PL1 to PAL1.

After 1500 cal yr BP, the maximum accumulation of sediments was lower than 4 m for each 500-year period and the depocenter stayed close to the modern mouth of the Argens River (Fig. 7C-E). The depocenter moved southward from 1500 to 1000 cal yr BP and shows a maximum thickness of 3-4 m at BN5 (Fig. 7C). The sediment thickness pattern between 1000 and 500 cal yr BP was quite similar to the previous period, with maximum values of 2-3 m (Fig. 7D). From 500 to 0 cal yr BP, the highest sediment accumulation occurred in two areas located, on the one hand, between Verteil and ESC1, and, on the other hand, close to the mouth of the Argens River around BN5 (Fig. 7E).

6.3. Elevation modelling and coastal palaeogeography

Deltaic areas with elevation above or below sea level correspond to subaerial or subaqueous delta, respectively (Anthony, 2015). The past sea levels are taken from Vacchi et al. (2016) (Table 2).

At 2500 cal yr BP, the elevation model reveals that the lower valley of the Argens River was largely occupied by a marine bay with a subaqueous delta extended until the Verteil site and a prodelta/delta front transition located between PL1 and PAL1 (Fig. 8A). The reduction in the surface area of the subaqueous delta between 2500 and 2000 cal yr BP was probably due to the progradation of the Argens, Reyran and Garonne rivers, which would have led to an eastward displacement of the prodelta/delta front transition between PAL1 and BN5 and to a decrease of the maximum depth of the marine bay from

621 ca. 15 to 10 m (Fig. 8A-B). Then the transition between the delta front and the prodelta
622 moved east of BN5 after 2000 cal yr BP (Fig. 8B-C).
623 During the first millennium CE, elevation models suggest that land emergence seems to
624 have been more important in the northern part of the ARDS, while subaqueous delta
625 environment would have persisted on the southern side of the ARDS between PAL1,
626 BN5 and VIL2 at the same time (Fig. 8B-D). The progradation in the southern part of the
627 ARDS occurred mainly during the last millennium and would have been characterized by
628 the formation of a fan-delta that grew between BN5 and VIL2 (Fig. 8D-E). Historical
629 maps show that the downstream flow of the Argens River was divided into two branches
630 at least from the end of the 16th century CE to the end of the 18th century CE (Cohen,
631 1997; Bertoncello et al., 2008, 2014a). In addition to the southern branch of the Argens
632 River, the Villepey River might also have contributed to the progradation in the southern
633 part of the delta system, as shown by maps from the 18th century CE (Bertoncello et al.,
634 2008, 2014a).
635 The transition from subaqueous to subaerial delta at PAL1 and BN1 occurred between
636 1000 and 500 cal yr BP. At 500 cal yr BP, the elevation model suggests that a large part
637 of the delta plain was above sea level, while a shallow body of water (< 1 m depth)
638 oriented in a NNE-SSW direction persisted along the coastline (Fig. 8E). Moreover, a
639 seaward progradation of ca. 1 km on average should have occurred between BN5 and
640 VIL2 during the last 500 years, which yields a mean progradation rate of 2 $m.yr^{-1}$.
641 The present topography of the coastal plain exhibits an area of lower elevation between
642 ESC1 and PL1 around the Garonne River, which is surrounded by two levees along the
643 Reyran River north of PAL1 and along the Argens River between Verteil and PAL1 (Fig.
644 1B). The elevation models suggest that these topographic features were largely
645 inherited over the past 2000 years (Fig. 8B-E). More specifically, the small shallow

depression above sea level south of ESC1 at 500 cal yr BP (Fig. 8E) is consistent with the palaeoecological and chronological data from the ESC1 core that shows the presence of a freshwater marsh from ca. 700 to 330 cal yr BP (Allinne et al., 2006).

7. DISCUSSION

7.1. Sediment flux and fluvial activity

The elevation models were used to estimate late Holocene sediment fluxes in the ARDS (Fig. 9a). The total sediment flux in the confined bayhead delta was greatest from 2500 to 2000 cal yr BP, with a deposition rate estimated at 52,000 ± 8500 $m^3.yr^{-1}$. A decrease in total sediment flux occurred after 2000 cal yr BP, with rates ranging from 15,800 ± 2300 to 26,700 ± 4100 $m^3.yr^{-1}$. The sediment flux in the unconfined bayhead delta along the modern delta front east of BN5 (Fig. 6) shows a general decrease from 47,900 ± 9600 to 27,000 ± 5400 $m^3.yr^{-1}$ over the last 2500 years (Fig. 9a).

Subaerial and subaqueous sediment fluxes in the confined bayhead delta were estimated by calculating the volume of sediments above and below sea level, respectively. The subaqueous sediment flux followed a similar trend to the total sediment flux. More specifically, the rates of subaqueous sediment flux declined sharply from 41,200 ± 8200 to 18,700 ± 3700 $m^3.yr^{-1}$ between 2500 and 1500 cal yr BP, then from 6200 ± 1200 to 700 ± 100 $m^3.yr^{-1}$ during the last millennium. Overall, the subaerial sediment flux exhibits an inverse trend with rates ranging from 8000 ± 1600 to 10,700 ± 2100 $m^3.yr^{-1}$ between 2500 and 500 cal yr BP, then increasing to 17,800 ± 3600 $m^3.yr^{-1}$ between 500 and 0 cal yr BP (Fig. 9a). Moreover, it is worth noting that the rate of subaerial sediment flux from 2500 to 2000 cal yr BP (10,700 ± 2100 $m^3.yr^{-1}$) was slightly higher than that from 2000 to 1500 cal yr BP (8000 ± 1600 $m^3.yr^{-1}$).

671 The subaqueous sediment flux was ca. 2 to 4 times higher than the subaerial sediment
672 flux between 2500 and 1500 cal yr BP, while the latter exceeded the former during the
673 last millennium. The subaerial sediment flux was 25 times higher than the subaqueous
674 sediment flux over the past 500 years. In fact, the rate of subaerial sediment flux
675 increased sharply between 500 and 0 cal yr BP and was two times higher than during
676 the period from 1000 to 500 cal yr BP. This sharp increase was associated with a slight
677 increase in the total sediment flux of the confined bayhead delta between 500 and 0 cal
678 yr BP, although this latter should be interpreted with caution given uncertainties of flux
679 rates. Besides, the sediment flux of the unconfined bayhead delta does not seem to have
680 significantly changed during the last millennium (Fig. 9a).
681 The high rates of sediment flux during the late Iron Age Cold Period (IACP) and the early
682 Roman Warm Period (RWP) between 2500 and 2000 cal yr BP were accompanied by
683 high levels of fluvial activity in the easternmost part of the lower Argens valley, as
684 suggested by the geochemical indicators of riverine input from the BN1 and BN5 cores
685 (Fig. 9b-c). The decrease in sediment fluxes between 2000 and 1500 cal yr BP was
686 contemporaneous with a period of low fluvial activity in the second half of the RWP.
687 Then the fluvial activity increased and was generally higher than average during the
688 Dark Ages Cold Period (DACP), the Medieval Warm Period (MWP) and the Little Ice Age
689 (LIA), except for BN5 over the last 300 years.
690 The periods of higher than average fluvial activity in the ARDS during the late Holocene
691 were most often associated with high riverine flooding in the southern French Alps and,
692 more generally, with more frequent river floods and extreme fluvial events in
693 southeastern France (Fig. 9b-f). Overall, the Mediterranean deltas grew slowly during
694 the Middle Ages, then high fluvial sediment supply to coast led to their rapid growth
695 after 500 cal yr BP (Anthony et al., 2014), i.e. during the LIA and 20th century global

696 warming. In the western Mediterranean, the LIA was generally characterized by more
697 frequent flooding and higher fluvial activity (Barriendos Vallve and Martin-Vide, 1998;
698 Wilhelm et al., 2012; Wirth et al., 2013; Benito et al., 2015a; Degeai et al., 2017). Besides,
699 Gutiérrez-Elorza and Pena-Monné (1998) found that climate-driven sediment
700 accumulation in valleys from northeastern Spain was more widespread during the IACP
701 than during the LIA, which is consistent with the pattern of total sediment flux in the
702 ARDS (Fig. 9a).
703
704 7.2. Autogenic control
705 Autogenic processes play an important role in controlling the stratigraphic architecture
706 of bayhead delta (Simms et al., 2018). For fluvio-deltaic systems developed in incised
707 valleys, geomorphologically-driven autogenic processes such as channel avulsion,
708 meander cutoff, increasing levee height and tributary junction can have been controlled
709 by changes in accommodation space and valley gradient, confluence of tributary valleys,
710 or channel extension (Vis et al., 2010; Amorosi et al., 2013a; Simms and Rodriguez,
711 2015; Simms et al., 2018).
712 In the lower valley of the Argens River, the evolution of subaqueous sediment fluxes
713 paralleled a progressive decrease in the mean slope of the longitudinal valley gradient
714 and in the volume of the accommodation space, which were higher than 2.8‰ and 20
715 Mm^3, respectively, between 2500 and 2000 cal yr BP (Fig. 10a-c). The general evolution
716 of the rates of subaqueous sediment deposition in the ARDS could therefore have been
717 primarily driven by geomorphic factors over the last 2500 years. In general, lower rates
718 of sediment flux into estuarine systems and late stages of sedimentary fill in a largely
719 infilled estuarine basin, i.e. in a shallow subaqueous environment, are controlled by
720 limited accommodation space rather than sediment flux (Clement and Fuller, 2018).

721 More specifically, the lowest rate of subaqueous sediment flux in the incised-valley
722 system of the Argens River would have been driven by a very limited accommodation
723 space over the last 500 years (Fig. 10b).
724 The sediment flux and fluvial activity associated with the marine environment of
725 prodelta in unit 1 (Fig. 2, 3), which spans the period from ca. 2700 to 1800 cal yr BP
726 from the age-elevation models (Fig. 6), were high in the late IACP then decreased during
727 the first half of the RWP (Fig. 10c-e). This is inconsistent with the environmental
728 evolution of western Mediterranean prodeltas, which generally show an upward
729 increase in riverine influence (Amorosi et al., 2008, 2013c). Therefore, the period of high
730 fluvial activity and sediment flux between 2500 and 2000 cal yr BP could be indicative of
731 an increased fluvial sedimentation caused by allogenic forcing rather than by autogenic
732 control during delta progradation.
733 By contrast, the increasingly strong riverine input in the easternmost part of the Argens
734 valley from ca. 1650 to 1300 cal yr BP corresponds to the formation of a delta front,
735 which suggests that sediment flux was mainly controlled by autogenic processes during
736 this period (Fig. 10e). Besides, a regional increase in riverine flood frequency occurred
737 in southeastern France during the DACP (Fig. 9d-f). Thus, the fluvial sediment supply
738 associated with the advancing delta front could have been strengthened by an increase
739 in riverine input in response to allogenic forcing (e.g. climate change).
740 The high fluvial activity of the DACP was maintained in the MWP from ca. 1100 to 600
741 cal yr BP (Fig. 10e). During the period between 1500 and 500 cal yr BP, the elevation
742 models suggest that delta progradation led to tributary junctions of the Argens, Reyran
743 and Villepey Rivers in the easternmost part of the lower Argens valley (Fig. 8C-E). In
744 general, the progradation rates of bayhead deltas increase when crossing
745 geomorphologically and environmentally controlled thresholds such as tributary

746 junctions in the absence of allogenic forcing mechanisms (Simms and Rodriguez, 2015).
747 Moreover, the fluvial sediments filling the river channels identified in BN1 and BN5
748 cores were deposited between ca. 1350 and 450 cal yr BP and between ca. 1000 and 550
749 cal yr BP, respectively (Fig. 2, 3, 6). Thus, the period of high fluvial activity during the
750 MWP could have been driven by autogenic processes such as tributary junction or
751 channel avulsion. Furthermore, each flood record in the southern Alps exhibits at least
752 one episode of more frequent riverine flooding during the MWP (Fig. 9d-e). Therefore, it
753 cannot be ruled out that the high levels of fluvial activity in the ARDS were partially
754 controlled by allogenic forcing during the MWP.
755 From 500 to 0 cal yr BP, the formation of the floodplain in the easternmost part of the
756 lower Argens valley was associated with the highest rate of subaerial sediment flux and
757 with higher than average levels of fluvial activity (Fig. 10d-e), although the mean slope
758 and accommodation space were very low (Fig. 10a-b). Besides, this period was
759 characterized by high flood frequency and fluvial activity in southeastern France (Fig.
760 9d-f). All this suggests that fluvial sedimentation in the ARDS was closely related to
761 allogenic factors during the LIA.
762
763 7.3. Impact of climate change
764 The impacts of rapid climate change on vegetation cover and hydrological regime are
765 allogenic factors that may have controlled the fluvial and coastal sedimentation in the
766 western Mediterranean during the Holocene (Fletcher and Zielhofer, 2013). At this time,
767 the periods of higher flood frequency in this region coincided with transitions to cool
768 and wet climatic conditions during persistent negative phases of the North Atlantic
769 oscillation (NAO) (Wirth et al., 2013; Benito et al., 2015a).

770 The NAO is one of the most prominent and recurrent modes of atmospheric circulation
771 variability in Europe (Hurrell et al., 2003). A southward (northward) shift of the North
772 Atlantic westerly winds and storm tracks during the negative (positive) phase of the
773 NAO leads to a wetter (drier) climate in southern Europe and to a drier (wetter) climate
774 in northern Europe (Hurrell, 1995; Serreze et al., 1997; Osborn et al., 1999; Trigo et al.,
775 2002). A well-known speleothem record of late Holocene climate change in northwest
776 Scotland (Fig. 1A) was supposedly driven by the bipolar seesaw of storminess and
777 humidity related to the NAO (Proctor et al., 2002; Trouet et al., 2009). In the lower
778 Argens valley, the episodes of high fluvial activity in the late IACP, the first half of the
779 RWP, the DACP and the LIA occurred during dry periods in northern Europe and should
780 thus have been associated with a southward shift of the westerly winds typically found
781 in a negative phase of the NAO (Fig. 10e-g, 11A), except for the MWP during which the
782 high fluvial activity was mainly driven by autogenic control due to delta progradation
783 (see section 7.2). However, increased flood frequencies in Europe may also have been
784 influenced by other small-scale flow patterns in the atmosphere (Jacobeit et al., 2003).
785 Hence, we undertook an empirical orthogonal function (EOF) analysis of winter
786 (December to February) sea level pressure (SLP) using the 500 yr data set from
787 Luterbacher et al. (2002) in order to highlight atmospheric circulation patterns in the
788 North Atlantic and Europe (Fig. 11). The respective contributions of the three first EOFs
789 to the total variance are estimated at 51, 20 and 14%. The leading EOF mode (EOF1)
790 exhibits a north-south dipole with zonal flow over Europe (Fig. 11A). This NAO-like
791 pattern is characterized by high (low) SLP anomalies over the Icelandic Low and low
792 (high) SLP anomalies over the Azores High during its negative (positive) phase
793 (Luterbacher et al., 2002; Josey et al., 2011), although its southern centre is offset to the
794 east (Fig. 1A, 11A). The second EOF mode (EOF2) shows anomalously low (high) SLP

795 over the North Sea that may be associated with the negative (positive) phase of the East
796 Atlantic/West Russian (EA/WR) pattern (Fig. 11B) (Josey et al., 2011). The third EOF
797 mode (EOF3) is characterized by high (low) SLP anomalies centred west of the British
798 Isles around 55°N latitude and 25°W longitude (Fig. 11C), which correspond to the
799 negative (positive) phase of the East Atlantic (EA) pattern (Luterbacher et al., 2002;
800 Josey et al., 2011).
801 The EA/WR and EA patterns were mentioned as potential drivers of atmospheric
802 circulation and climate change in western Europe during the late Holocene (Dermody et
803 al., 2012; Moffa-Sanchez et al., 2014; Sanchez-Lopez et al., 2016; Sicre et al., 2016;
804 Degeai et al., 2017). From observational data, the negative phases of the EA/WR and EA
805 patterns were associated with higher precipitation and enhanced ocean heat loss in the
806 northwestern Mediterranean (Qian et al., 2000; Josey et al., 2011), while strong (weak)
807 surface winds in France were associated with either a negative (positive) phase of the
808 EA/WR pattern or a positive (negative) phase of the EA pattern (Najac et al., 2009).
809 Hence, given the late Holocene storm activity in France and the SST record in the
810 northwestern Mediterranean (Fig. 10h-k), the late IACP should have been characterized
811 by a negative phase of the EA pattern, then the lower RWP (upper RWP-DACP) and
812 MWP (LIA) would have been associated with a positive (negative) phase of the EA/WR
813 pattern (Fig. 10l).
814 In the northwestern Mediterranean, the coupling of cold northerly winds generated by
815 winter North Atlantic blocking events due to anomalously high SLP in the eastern North
816 Atlantic during the negative phase of the EA pattern (Shabbar et al., 2001; Jiang et al.,
817 2003; Trigo et al., 2004; Josey et al., 2011; Moffa-Sanchez et al., 2014; Sanchez-Lopez et
818 al., 2016; Sicre et al., 2016) with warm and dry summer due to the northward position of
819 the ITCZ (Goudeau et al., 2015) could have led to enhanced convection and higher

820 rainfall along the southern Alps in the late IACP (Fig. 10l-m, 11C), similarly to modern
821 heavy precipitating systems over southeastern France (Nuissier et al., 2008; Duffourg
822 and Ducrocq, 2011). This synoptic situation could explain the high fluvial activity and
823 sediment flux in the ARDS during the late IACP (Fig. 10e).
824 The positive phase of the EA/WR pattern in the lower RWP from ca. 2300 to 1800 cal yr
825 BP was associated with a large-scale circulation pattern characterized by a negative or
826 positive phase of the NAO (Fig. 10g, l). This period shows a decreasing trend in fluvial
827 activity in the ARDS apart from the 2nd and 1st centuries BCE (Fig. 10e). The ITCZ was
828 still in a northern position during the lower RWP, but the absence or low frequency of
829 atmospheric blocking events and cold northerly winds would have limited atmospheric
830 convection and precipitation in the southern Alps at this time. During the late RWP and
831 the DACP from 1800 to 1150 cal yr BP, the negative phase of the EA/WR pattern
832 corresponded to a general increase in fluvial activity in the ARDS, with higher than
833 average values when the negative phases of the EA/WR and NAO patterns were coupled
834 in the late DACP between 1600 and 1150 cal yr BP (Fig. 10e, g, l, 11B).
835 In the Western Mediterranean, there is a broad consensus on the climatic conditions of
836 the MWP (LIA), which were generally warm (cold) and dry (wet) from continental
837 records in Spain (Martin-Puertas et al., 2008, 2010; Martin-Chivelet et al., 2011; Moreno
838 et al., 2012; Sanchez-Lopez et al., 2016), Italy (Frisia et al., 2005; Mensing et al., 2016;
839 Sadori et al., 2016), southern France (Degeai et al., 2017) and northern Morocco
840 (Wassenburg et al., 2013). Overall, the MWP (LIA) would have been characterized by the
841 combination of a positive (negative) phase of the NAO with a positive (negative) phase
842 of the EA/WR pattern (Fig. 10g, l).
843 The climatic context of the LIA would have been similar to that of the DACP (Fig. 11B).
844 During the cold and humid period of the LIA, high detrital inputs of terrigenous material

were identified in marine sediments from the western Mediterranean basin (Fig. 1A). Interestingly, the sharp increase in subaerial sediment flux in the ARDS after 500 cal yr BP is consistent with this high offshore discharge of riverine sediment (Fig. 10d). Overall, the LIA was characterized by high fluvial sediment supply to Mediterranean deltas in an increasingly human-influenced environment (Anthony et al., 2014). However, it is currently difficult to assess the real contribution of human land use to late Holocene sediment flux in the ARDS because of the lack of quantitative data to measure the magnitude of the geomorphic impact of anthropogenic forcing.

Finally, the climate-driven fluvial activity in the ARDS over the past 2500 years would have been higher than average when the negative phase of the NAO-like pattern was associated with either a negative phase of the EA/WR pattern or the combination of a negative EA pattern with a northward migration of the ITCZ.

8. CONCLUSION

The elevation modelling and palaeogeographic reconstruction of incised valleys in coastal areas is challenging because this kind of environment is often characterized by rapid changes in relative sea level, shoreline progradation, delta sedimentation and climatic conditions. A new multi-method approach using cores and archaeological trenches, geochemistry and magnetic susceptibility of sediments, malacology, radiocarbon chronology, geostatistics and numerical modelling was undertaken in order to robustly characterize changes in environmental conditions, geomorphic setting and sediment flux associated with delta growth in incised-valley systems. This quantitative method was applied to the bayhead delta of the Argens River in the western

Mediterranean, in order to assess the impacts of autogenic control and climate change on the variations in sediment flux and fluvial activity of this deltaic system.

The coastal dynamics of the Argens River delta system were studied over the last 2500 years. The sedimentary successions of this deltaic depositional system revealed four major facies associations from bottom to top: (1) a prodelta with clay-sand alternations deposited in a marine environment with brackish or freshwater influences and high levels of salinity, (2) a delta front characterized by higher sand content as well as by coarsening-upward trend and gradual increase in riverine input, (3) river channels filled with sand and gravel, and (4) a floodplain with a high abundance of land snails and low salinity levels.

Late Holocene sediment fluxes were estimated from numerical modelling then compared with hydroclimate proxy records and geomorphic factors. An overall decrease in subaqueous sediment supply over the last 2500 years could have been geomorphologically controlled by autogenic processes such as changes in accommodation space and delta slope. High rates of sediment flux between 2500 and 2000 cal yr BP coincided with higher precipitation and more frequent riverine flooding in the western Mediterranean. The maximum rate of subaerial sediment flux from 500 to 0 cal yr BP could have been caused by higher fluvial activity and more frequent flood events during the cold and wet climatic conditions of the Little Ice Age.

In general, the high sediment fluxes at 2500-2000 and 500-0 cal yr BP were associated with higher than average levels of fluvial activity in the Argens River delta system. The periods of high fluvial activity driven by climate change were associated with a southward shift of the North Atlantic westerlies and storm tracks in southern Europe. This atmospheric circulation pattern was combined with either (1) a negative phase of the East Atlantic pattern coupled to a northward migration of the intertropical

convergence zone in the late Iron Age Cold Period, or (2) a negative phase of the East Atlantic/West Russian pattern during the Dark Ages Cold Period and Little Ice Age. This quantitative approach will need to be applied to other Mediterranean deltas in order to compare the variation of coastal sediment fluxes in response to hydroclimate change and geomorphic setting over the past millennia. Besides, the study of other deltaic sequences will be needed to firmly establish a link between delta sedimentation and atmospheric circulation patterns in the western Mediterranean. Furthermore, the analysis of palaeobotanical, archaeological and historical data will be required to accurately estimate the impact of human land use on sediment flux and geomorphic change in these coastal areas.

Acknowledgments

This work is a part of a research program financially supported by the CNRS and the French Ministry of Culture and Communication. The BN1 and BN5 cores were undertaken by the CETE Méditerranée, the C2FN (DT INSU, CNRS, EQUIPEX CLIMCOR, Investissements d'Avenir ANR-11-EQPX-0009) and the BRGM. The sedimentological analyses were done at the ArcheoEnvironnement Laboratory (CNRS UMR5140). We thank Dr. Edward Anthony (editor) and two anonymous reviewers for their helpful remarks and suggestions that improved the manuscript.

Data availability

http://dx.doi.org/10.17632/p5fbtmwnsr.1

919 References

920

921 Allinne, C., Devillers, B., Bertoncello, F., Bouby, L., Bruneton, H., Bui Thi, M., Cade, C.,
922 Revil, A., 2006. Archéologie et paléoenvironnement sur le site du pont romain des
923 Esclapes (Fréjus, Var). *ArcheoSciences* 30, 181-196.
924 Amorosi, A., Milli, S., 2001. Late Quaternary depositional architecture of Po and Tevere
925 river deltas (Italy) and worldwide comparison with coeval deltaic successions.
926 *Sediment. Geol.* 144, 357-375.
927 Amorosi, A., Centineo, M.C., Colalongo, M.L., Fiorini, F., 2005. Millennial-scale
928 depositional cycles from the Holocene of the Po Plain, Italy. *Mar. Geol*. 222-223, 7-18.
929 Amorosi, A., Dinelli, E., Rossi, V., Vaiani, S.C., Sacchetto, M., 2008. Late Quaternary
930 palaeoenvironmental evolution of the Adriatic coastal plain and the onset of Po River
931 Delta. *Palaeogeogr. Palaeoclim. Palaeoecol.* 268, 80-90.
932 Amorosi, A., Lucchi, M.R., Rossi, V., Sarti, G., 2009. Climate change signature of small-
933 scale parasequences from Lateglacial–Holocene transgressive deposits of the Arno
934 valley fill. *Palaeogeogr. Palaeoclim. Palaeoecol.* 273, 142-152.
935 Amorosi, A., Bini, M., Giacomelli, S., Pappalardo, M., Ribecai, C., Rossi, V., Sammartino, I.,
936 Sarti, G., 2013a. Middle to late Holocene environmental evolution of the Pisa coastal
937 plain (Tuscany, Italy) and early human settlements. *Quat. Int*. 303, 93-106.
938 Amorosi, A., Rossi, V., Sarti, G., Mattei, R., 2013b. Coalescent valley fills from the late
939 Quaternary record of Tuscany (Italy). *Quat. Int.* 288, 129-138.
940 Amorosi, A., Rossi, V., Vella, C., 2013c. Stepwise post-glacial transgression in the Rhône
941 Delta area as revealed by high-resolution core data. *Palaeogeogr. Palaeoclim.*
942 *Palaeoecol.* 374, 314-326.

943 Amorosi, A., Bracone, V., Campo, B., D'Amico, C., Rossi, V., Rosskopf, C.M., 2016. A late
944 Quaternary multiple paleovalley system from the Adriatic coastal plain (Biferno
945 River, Southern Italy). *Geomorphology* 254, 146-159.
946 Anthony, E.J., 2015. Wave influence in the construction, shaping and destruction of river
947 deltas: a review. *Mar. Geol.* 361, 53-78.
948 Anthony, E.J., Marriner, N., Morhange, C., 2014. Human influence and the changing
949 geomorphology of Mediterranean deltas and coasts over the last 6000 years: From
950 progradation to destruction phase? *Earth Sci. Rev.* 139, 336-361.
951 Arnaud-Fassetta, G., Carcaud, N., Castanet, C., Salvador, P.-G., 2010. Fluviatile
952 palaeoenvironments in archaeological context: Geographical position, methodological
953 approach – Hydrological risk issues. *Quat. Int.* 216, 93-117.
954 Barriendos Vallve, M., Martin-Vide, J., 1998. Secular climatic oscillations as indicated by
955 catastrophic floods in the Spanish Mediterranean coastal area (14th–19th centuries).
956 *Climatic Change* 38, 473-491.
957 Benito, G., Macklin, M.G., Zielhofer, C., Jones, A.F., Machado, M.J., 2015a. Holocene
958 flooding and climate change in the Mediterranean. *Catena* 130, 13-33.
959 Benito, G., Macklin, M.G., Panin, A., Rossato, S., Fontana, A., Jones, A.F., Machado, M.J.,
960 Matlakhova, E., Mozzi, P., Zielhofer, C., 2015b. Recurring flood distribution patterns
961 related to short-term Holocene climatic variability. *Sci. Rep.* 5(16398), 1-8.
962 Bertoncello, F., Bonnet, S., Bouby, L., Delhon, C., Devillers, B., Guillon, S., 2008. *Projet*
963 *Collectif de Recherches « Occupation du sol et patrimoine archéologique dans la basse*
964 *vallée de l'Argens ». Rapport de fin de projet*. Rapport pour le Ministère de la Culture et
965 de la Communication, CEPAM, Nice, 124 p.
966 Bertoncello, F., Bonnet, S., Excoffon, P., Bony, G., Morhange, C., Gébara, C., Georges, K.,
967 Devillers, B., 2011. Dynamique du littoral et peuplement : le cas de la colonie romaine

de Fréjus. *In* Pasqualini, M. (Ed.): *Fréjus romaine, la ville et son territoire. Agglomérations de Narbonnaise, des Alpes-Maritimes et de Cisalpine à travers la recherche archéologique*. Editions APDCA, Antibes, 75-87.

Bertoncello, F., Fovet, E., Tannier, C., Gandini, C., Lautier, L., Nouvel, P., Nuninger, L., 2012. Configurations spatiales et hiérarchiques du peuplement antique : des indicateurs quantitatifs pour une confrontation interrégionale. *In* Bertoncello, F., Braemer, F. (Eds.): *Variabilités Environnementales, Mutations sociales : Nature, Intensités, Échelles et Temporalités des changements*. Editions APDCA, Antibes, 175-190.

Bertoncello, F., Devillers, B., Bonnet, S., Guillon, S., Bouby, L., Delhon, C., 2014a. Mobilité des paysages littoraux et peuplement dans la basse vallée de l'Argens (Var, France) au cours de l'Holocène. *Quaternaire* 25 (1), 23-44.

Bertoncello, F., Burri, S., Delhon, C., Digelmann, P., Bernigaud, N., Borréani, M., Gébara, C., Portalier, N., Purdue, L., 2014b. *Projet Collectif de Recherches « Dynamiques du peuplement et des paysages dans le territoire de Fréjus ». Rapport d'activité 2014 et projet 2015-2016*. Rapport pour le Ministère de la Culture et de la Communication, CEPAM, Nice, 38 p.

Bertoncello, F., Bernigaud, N., Burri, S., Degeai, J.-P., Delhon, C., Digelmann, P., Gayet, F., Jansen, P., Mercuri, L., Ouriachi, M.-J., Porra, M., Portalier, N., Purdue, L., Romagnan, B., Segura, J.-A., Vaschalde, C., 2016. *Projet Collectif de Recherches, Dynamiques du peuplement et des paysages dans le territoire de Fréjus. Rapport final 2014-2016*. Rapport pour le Ministère de la Culture et de la Communication, CEPAM, Nice, 115 p.

Bony, G., Morhange, C., Bruneton, H., Carbonel, P., Gébara, C., 2011. 2000 ans de colmatage du port antique de Fréjus (*Forum Julii*), France : une double métamorphose littorale. *CR Geosci.* 343, 701-715.

993 Chagué-Goff, C., Dawson, S., Goff, J.R., Zachariasen, J., Berryman, K.R., Garnett, D.L.,
994 Waldron, H.M., Mildenhall, D.C., 2002. A tsunami (ca. 6300 years BP) and other
995 Holocene environmental changes, northern Hawke's Bay, New Zealand. *Sediment.*
996 *Geol.* 150, 89-102.
997 Clement, A.J.H., Fuller, I.C., 2018. Influence of system controls on the Late Quaternary
998 geomorphic evolution of a rapidly-infilled incised-valley system: The lower
999 Manawatu valley, North Island New Zealand. *Geomorphology* 303, 13-29.
1000 Cohen, O., 1997. La baie de Fréjus : 2000 ans d'évolution du rivage. *Mappemonde* 1, 6-12.
1001 Croudace, I.W., Rindby, A., Rothwell, R.G., 2006. ITRAX: description and evaluation of a
1002 new multi-function X-ray core scanner. *In* Rothwell, R.G. (ed.): *New techniques in*
1003 *sediment core analysis*. Geological Society, London, Special Publications 267, 51-63.
1004 Dalrymple, R.W., Zaitlin, B.A., Boyd, R., 1992. Estuarine facies models: conceptual basis
1005 and stratigraphic implications. *J. Sediment. Petrol.* 62 (6), 1130-1146.
1006 Dearing, J., 1999. *Environmental magnetic susceptibility using the Bartington MS2 system*.
1007 Bartington Instruments, Oxford, 43 p.
1008 Degeai, J.-P., Devillers, B., Dezileau, L., Oueslati, H., Bony, G., 2015. Major storm periods
1009 and climate forcing in the Western Mediterranean during the Late Holocene. *Quat. Sci.*
1010 *Rev.* 129, 37-56.
1011 Degeai, J.-P., Devillers, B., Blanchemanche, P., Dezileau, L., Oueslati, H., Tillier, M., Bohbot,
1012 H., 2017. Fluvial response to the last Holocene rapid climate change in the
1013 Northwestern Mediterranean coastlands. *Glob. Planet. Chang.* 152, 176-186.
1014 Delile, H., Abichou, A., Gadhoum, A., Goiran, J.-P., Pleuger, E., Monchambert, J.-Y., Wilson,
1015 A., Fentress, E., Quinn, J., Ben Jerbania, I., Ghozzi, F., 2015. The geoarchaeology of
1016 Utica, Tunisia: the paleogeography of the Mejerda Delta and hypotheses concerning
1017 the location of the ancient harbour. *Geoarchaeology* 30, 291-306.

1018 Dermody, B.J., De Boer, H.J., Bierkens, M.F.P., Weber, S.L., Wassen, M.J., Dekker, S.C., 2012.
1019 A seesaw in Mediterranean precipitation during the Roman Period linked to
1020 millennial-scale changes in the North Atlantic. *Clim. Past* 8, 637-651.
1021 Devillers, B., Bonnet, S., 2006. 6000 ans d'histoire environnementale de la lagune de
1022 Villepey (Fréjus, Var) : premiers résultats de l'étude multi-proxies de la carotte Vil2.
1023 *ArcheoSciences* 30, 197-203.
1024 Devillers, B., Excoffon, P., Morhange, C., Bonnet, S., Bertoncello, F., 2007. Relative sea-
1025 level changes and coastal evolution at *Forum Julii* (Fréjus, Provence). *CR Geosci.* 339,
1026 329-336.
1027 Devillers, B., Bony, G., Degeai, J.-P., Gasco, J., Lachenal, T., Bruneton, H., Yung, F., Oueslati,
1028 H., Thierry, A., 2019. Holocene coastal environmental changes and human occupation
1029 of the lower Hérault River, southern France. *Quat. Sci. Rev.* 222, 105912.
1030 Dezileau, L., Sabatier, P., Blanchemanche, P., Joly, B., Swingedouw, D., Cassou, C.,
1031 Castaings, J., Martinez, P., Von Grafenstein, U., 2011. Intense storm activity during the
1032 Little Ice Age on the French Mediterranean coast. *Palaeogeogr. Palaeoclim. Palaeoecol.*
1033 299, 289-297.
1034 Dezileau, L., Pérez-Ruzafa, A., Blanchemanche, P., Degeai, J.-P., Raji, O., Martinez, P.,
1035 Marcos, C., Von Grafenstein, U., 2016. Extreme storms during the last 6500 years from
1036 lagoonal sedimentary archives in the Mar Menor (SE Spain). *Clim. Past* 12, 1389-1400.
1037 Dubar, M., 2004. L'édification de la plaine deltaïque du Bas Argens (Var, France) durant
1038 la Protohistoire et l'Antiquité. Application d'un modèle numérique 2D à l'archéologie.
1039 *Méditerranée* 102, 47-54.
1040 Dubar M., Anthony, E.J., 1995. Holocene environmental change and river-mouth
1041 sedimentation in the Baie des Anges, French Riviera. *Quat. Res.* 43, 329-343.

1042 Dubar, M., Bui-Thi, M., Nicol-Pichard, S., Thinon, M., 2004. Étude palynologique du
1043 carottage de Pont d'Argens (Roquebrune-sur-Argens, Var) : histoire holocène de la
1044 végétation en Provence cristalline ; facteurs naturels et anthropiques. *Ecologia*
1045 *Mediterranea* 30 (2), 147-157.
1046 Duffourg, F., Ducrocq, V., 2011. Origin of the moisture feeding the Heavy Precipitating
1047 Systems over Southeastern France. *Nat. Hazards Earth Syst. Sci.* 11, 1163-1178.
1048 Durozoy, G., Gouvernet, C., Jonquet, P., Theillier, P., 1970. *Inventaire des ressources*
1049 *hydrauliques dans la basse vallée de l'Argens (Var)*. BRGM, Orléans, 39 p.
1050 EPA, 2007. *Method 6200: Field portable X-ray fluorescence spectrometry for the*
1051 *determination of elemental concentrations in soil and sediment*. United Stated
1052 Environmental Protection Agency, 32 p.,
1053 https://www.epa.gov/sites/production/files/2015-12/documents/6200.pdf
1054 Excoffon, P., Devillers, B., Bonnet, S., Bouby, L., 2006. Nouvelles données sur la position
1055 du littoral antique de Fréjus. Le diagnostic archéologique du "théâtre
1056 d'agglomération" (Fréjus, Var). *ArcheoSciences* 30, 205-221.
1057 Excoffon, P., Bonnet, S., Devillers, B., Berger, J.-F., 2010. L'évolution de trait de côte aux
1058 abords de Fréjus, de sa foundation jusqu'à la fin du I^{er} siècle après J.-C. In: Delestre, X.,
1059 Marchesi, H. (Eds.), *Archéologie des rivages méditerranéens : 50 ans de recherche. Actes*
1060 *du colloque d'Arles (Bouches-du-Rhône) 28-29-30 octobre 2009*. Errance, Paris, 47-53.
1061 Fletcher, W.J., Zielhofer, C., 2013. Fragility of Western Mediterranean landscapes during
1062 Holocene Rapid Climate Changes. *Catena* 103, 16-29.
1063 Fletcher, W.J., Debret, M., Sanchez-Goni, M.F., 2013. Mid-Holocene emergence of a low-
1064 frequency millennial oscillation in western Mediterranean climate: Implications for
1065 past dynamics of the North Atlantic atmospheric westerlies. *The Holocene* 23(2), 153-
1066 166.

1067 Fontugne, M., 2004. Les derniers progrès du calibrage des âges radiocarbone
1068 permettent-ils une révision des chronologies entre 25 et 50.000 ans B.P. ?
1069 *Quaternaire* 15 (3), 245-252.
1070 Frigola, J., Moreno, A., Cacho, I., Canals, M., Sierro, F.J., Flores, J.A., Grimalt, J.O., Hodell,
1071 D.A., Curtis, J.H., 2007. Holocene climate variability in the western Mediterranean
1072 region from a deepwater sediment record. *Paleoceanography* 22, PA2209.
1073 Frisia, S., Borsato, A., Spötl, C., Villa, I.M., Cucchi, F., 2005. Climate variability in the SE
1074 Alps of Italy over the past 17 000 years reconstructed from a stalagmite record.
1075 *Boreas* 34, 445-455.
1076 Gascou, J., 1982. Quand la colonie de Fréjus fut-elle fondée ? *Latomus* 41(1), 132-145.
1077 Gascou, J., Janon, M., 1985. Inscriptions Latines de Narbonnaise (I.L.N.)- Fréjus. *Gallia*
1078 Suppl. 44, 229 p.
1079 Gébara, C., Morhange, C., 2010. Fréjus (*Forum Julii*): le port antique/the ancient harbour.
1080 *J. Roman Archaeol*. Suppl. 77, 152 p.
1081 Giaime, M., Marriner, N., Morhange, C., 2019. Evolution of ancient harbours in deltaic
1082 contexts: a geoarchaeological typology. *Earth Sci. Rev.* 191, 141-167.
1083 Giraudi, C., Tata, C., Paroli, L., 2009. Late Holocene Evolution of Tiber River Delta and
1084 Geoarchaeology of Claudius and Trajan Harbor, Rome. *Geoarchaeology* 24 (3), 371-
1085 382.
1086 Goudeau, M.-L.S., Grauel, A.-L., Tessarolo, C., Leider, A., Chen, L., Bernasconi, S.M.,
1087 Versteegh, G.J.M., Zonneveld, K.A.F., Boer, W., Alonso-Hernandez, C.M., De Lange, G.J.,
1088 2014. The Glacial–Interglacial transition and Holocene environmental changes in
1089 sediments from the Gulf of Taranto, central Mediterranean. *Mar. Geol.* 348, 88-102.
1090 Goudeau, M.-L.S., Reichart, G.-J., Wit, J.C., De Nooijer, L.J., Grauel, A.-L., Bernasconi, S.M.,
1091 De Lange, G.J., 2015. Seasonality variations in the Central Mediterranean during

climate change events in the Late Holocene. *Palaeogeogr. Palaeoclim. Palaeoecol.* 418, 304-318.

Grimm, E.C., 1987. Coniss: a Fortran 77 program for stratigraphically constrained cluster analysis by the method of incremental sum of squares. *Comput. Geosci.* 13 (1), 13-35.

Grove, A.T., 2001. The "Little Ice Age" and its geomorphological consequences in Mediterranean Europe. *Climatic Change* 48, 121-136.

Gutiérrez-Elorza, M., Pena-Monné, J.L., 1998. Geomorphology and late Holocene climatic change in Northeastern Spain. *Geomorphology* 23, 205-217.

Haenssler, E., Nadeau, M.-J., Vött, A., Unkel, I., 2013. Natural and human induced environmental changes preserved in a Holocene sediment sequence from the Etoliko Lagoon, Greece: New evidence from geochemical proxies. *Quat. Int.* 308-309, 89-104.

Hurrell, J.W., 1995. Decadal trends in the North Atlantic Oscillation: regional temperatures and precipition. *Science* 269, 676-679.

Hurrell, J.W., Kushnir, Y., Ottersen, G., Visbeck, M., 2003. An overview of the North Atlantic Oscillation. In: Hurrell, J.W., Kushnir, Y., Ottersen, G., Visbeck, M. (Eds.), *The North Atlantic Oscillation: Climatic significance and environmental impact*. American Geophysical Union, Washington D.C., Geophysical Monograph 134, 1-35.

Jacobeit, J., Glaser, R., Luterbacher, J., Wanner, H., 2003. Links between flood events in central Europe since AD 1500 and large-scale atmospheric circulation modes. *Geophys. Res. Lett.* 30 (4), 1172.

Jalali, B., Sicre, M.-A., Bassetti, M.-A., Kallel, N., 2016. Holocene climate variability in the North-Western Mediterranean Sea (Gulf of Lions). *Clim. Past* 12, 91-101.

Jiang, Q., Smith, R.B., Doyle, J., 2003. The nature of the mistral: Observations and modelling of two MAP events. *Q. J. Roy. Meteorol. Soc.* 129, 857-875.

1116 Josey, S.A., Somot, S., Tsimplis, M., 2011. Impacts of atmospheric modes of variability on
1117 Mediterranean Sea surface heat exchange. *J. Geophys. Res.-Oceans* 116, C02032.
1118 Koster, K., Stafleu, J., Cohen, K.M., 2017. Generic 3D interpolation of Holocene base-level
1119 rise and provision of accommodation space, developed for the Netherlands coastal
1120 plain and infilled palaeovalleys. *Basin Res.* 29, 775-797.
1121 Lambeck, K., Bard, E., 2000. Sea-level change along the French Mediterranean coast for
1122 the past 30 000 years. *Earth Planet. Sci. Lett.* 175, 203-222.
1123 Lopez-Buendia, A.M., Bastida, J., Querol, X., Whateley, M.K.G., 1999. Geochemical data as
1124 indicators of palaeosalinity in coastal organic-rich sediments. *Chem. Geol.* 157, 235-
1125 254.
1126 Luterbacher, J., Xoplaki, E., Dietrich, D., Rickli, R., Jacobeit, J., Beck, C., Gyalistras, D.,
1127 Schmutz, C., Wanner, H., 2002. Reconstruction of sea level pressure fields over the
1128 Eastern North Atlantic and Europe back to 1500. *Clim. Dynam.* 18, 545-561.
1129 Makclin, M.G., Benito, G., Gregory, K.J., Johnstone, E., Lewin, J., Michczynska, D.J., Soja, R.,
1130 Starkel, L., Thorndycraft, V.R., 2006. Past hydrological events reflected in the
1131 Holocene fluvial record of Europe. *Catena* 66, 145-154.
1132 Martin-Chivelet, J., Munoz-Garcia, M.B., Edwards, R.L., Turrero, M.J., Ortega, A.I., 2011.
1133 Land surface temperature changes in Northern Iberia since 4000 yr BP, based on
1134 δ13C of speleothems. *Glob. Planet. Change* 77, 1-12.
1135 Martinez-Ruiz, F., Kastner, M., Gallego-Torres, D., Rodrigo-Gamiz, M., Nieto-Moreno, V.,
1136 Ortega-Huertas, M., 2015. Paleoclimate and paleoceanography over the past 20,000
1137 yr in the Mediterranean Sea Basins as indicated by sediment elemental proxies. *Quat.*
1138 *Sci. Rev.* 107, 25-46.

1139 Martin-Puertas, C., Valero-Garcés, B.L., Mata, M.P., Gonzalez-Sampériz, P., Bao, R.,
1140 Moreno, A., Stefanova, V., 2008. Arid and humid phases in southern Spain during the
1141 last 4000 years: the Zonar Lake record, Cordoba. *Holocene* 18 (6), 907-921.
1142 Martin-Puertas, C., Jiménez-Espejo, F., Martinez-Ruiz, F., Nieto-Moreno, V., Rodrigo, M.,
1143 Mata, M.P., Valero-Garcés, B.L., 2010. Late Holocene climate variability in the
1144 southwestern Mediterranean region: an integrated marine and terrestrial
1145 geochemical approach. *Clim. Past* 6, 807-816.
1146 Martin-Puertas, C., Valero-Garcés, B.L., Mata, M.P., Moreno, A., Giralt, S., Martinez-Ruiz, F.,
1147 Jiménez-Espejo, F., 2011. Geochemical processes in a Mediterranean Lake: a high-
1148 resolution study of the last 4,000 years in Zonar Lake, southern Spain. *J. Paleolimnol.*
1149 46, 405-421.
1150 Melis, R.T., Di Rita, F., French, C., Marriner, N., Montis, F., Serreli, G., Sulas, F., Vacchi, M.,
1151 2018. 8000 years of coastal changes on a western Mediterranean island: A multiproxy
1152 approach from the Posada plain of Sardinia. *Mar. Geol.* 403, 93-108.
1153 Mensing, S., Tunno, I., Cifani, G., Passigli, S., Noble, P., Archer, C., Piovesan, G., 2016.
1154 Human and climatically induced environmental change in the Mediterranean during
1155 the Medieval Climate Anomaly and Little Ice Age: A case from central Italy.
1156 *Anthropocene* 15, 49-59.
1157 Milli, S., D'Ambrogi, C., Bellotti, P., Calderoni, G., Carboni, M.G., Celant, A., Di Bella, L., Di
1158 Rita, F., Frezza, V., Magri, D., Pichezzi, R.M., Ricci, V., 2013. The transition from wave-
1159 dominated estuary to wave-dominated delta: The Late Quaternary stratigraphic
1160 architecture of Tiber River deltaic succession (Italy). *Sediment. Geol.* 284-285, 159-
1161 180.

1162 Moffa-Sanchez, P., Born, A., Hall, I.R., Thornalley, D.J.R., Barker, S., 2014. Solar forcing of
1163 North Atlantic surface temperature and salinity over the past millennium. *Nat. Geosci.*
1164 7, 275-278.
1165 Moreno, A., Pérez, A., Frigola, J., Nieto-Moreno, V., Rodrigo-Gámiz, M., Martrat, B.,
1166 González-Sampériz, P., Morellón, M., Martín-Puertas, C., Corella, J.P., Belmonte, A.,
1167 Sancho, C., Cacho, I., Herrera, G., Canals, M., Grimalt, J.O., Jiménez-Espejo, F., Martínez-
1168 Ruiz, F., Vegas-Vilarrúbia, T., Valero-Garcés, B.L., 2012. The Medieval Climate
1169 Anomaly in the Iberian Peninsula reconstructed from marine and lake records. *Quat.*
1170 *Sci. Rev.* 43, 16-32.
1171 Morhange, C., Marriner, N., Excoffon, P., Bonnet, S., Flaux, C., Zibrowius, H., Goiran, J.-P., El
1172 Amouri, M., 2013. Relative sea-level changes during Roman times in the Northwest
1173 Mediterranean: the 1st century A.D. fish tank of *Forum Julii*, Fréjus, France.
1174 *Geoarchaeology* 28 (4), 363-372.
1175 Morhange, C., Marriner, N., 2015. Archeological and biological relative sea-level
1176 indicators. *In* Shennan, I., Long, A.J., Horton, B.P. (Eds): *Handbook of sea-level research*.
1177 AGU, Wiley, Wiley Works Series, 146-156.
1178 Najac, J., Boé, J., Terray, L., 2009. A multi-model ensemble approach for assessment of
1179 climate change impact on surface winds in France. *Clim. Dynam.* 32, 615-634.
1180 Nieto-Moreno, V., Martinez-Ruiz, F., Giralt, S., Jiménez-Espejo, F., Gallego-Torres, D.,
1181 Rodrigo-Gamiz, M., Garcia-Orellana, J., Ortega-Huertas, M., de Lange, G.J., 2011.
1182 Tracking climate variability in the western Mediterranean during the Late Holocene:
1183 a multiproxy approach. *Clim. Past* 7, 1395-1414.
1184 Nieto-Moreno, V., Martinez-Ruiz, F., Giralt, S., Gallego-Torres, D., Garcia-Orellana, J.,
1185 Masqué, P., Ortega-Huertas, M., 2013a. Climate imprints during the 'Medieval Climate

Anomaly' and the 'Little Ice Age' in marine records from the Alboran Sea basin. *The Holocene* 23 (9), 1227-1237.

Nieto-Moreno, V., Martinez-Ruiz, F., Willmott, V., Garcia-Orellana, J., Masqué, P., Sinninghe Damsté, J.S., 2013b. Climate conditions in the westernmost Mediterranean over the last two millennia: An integrated biomarker approach. *Org. Geochem.* 55, 1-10.

Nuissier, O., Ducrocq, V., Ricard, D., Lebeaupin, C., Anquetin, S., 2008. A numerical study of three catastrophic precipitating events over southern France. I: Numerical framework and synoptic ingredients. *Q. J. Roy. Meteorol. Soc.* 134, 111-130.

Osborn, T.J., Briffa, K.R., Tett, S.F.B., Jones, P.D., Trigo, R.M., 1999. Evaluation of the North Atlantic Oscillation as simulated by a coupled climate model. *Clim. Dynam.* 15, 586-702.

Paillard, D., Labeyrie, L., Yiou, P., 1996. Macintosh program performs time-series analysis. *EOS Transactions AGU* 77 (39), 379-379.

Peltier, W.R., 2004. Global glacial isostasy and the surface of the ice-age Earth: The ICE-5G (VM2) model and GRACE. *Annu. Rev. Earth Planet. Sci.* 32, 111-149.

Proctor, C.J., Baker, A., Barnes, W.L., 2002. A three thousand year record of North Atlantic climate. *Clim. Dynam.* 19, 449-454.

Qian, B., Corte-Real, J., Xu, H., 2000. Is the North Atlantic Oscillation the most important atmospheric pattern for precipitation in Europe? *J. Geophys. Res.* 105, 11,901-11,910.

Reimer, P.J., Bard, E., Bayliss, A., Beck, J.W., Blackwell, P.G., Ramsey, C.B., Buck, C.E., Cheng, H., Edwards, R.L., Friedrich, M., Grootes, P.M., Guilderson, T.P., Haflidason, H., Hajdas, I., Hatté, C., Heaton, T.J., Hoffmann, D.L., Hogg, A.G., Hughen, K.A., Kaiser, K.F., Kromer, B., Manning, S.W., Niu, M., Reimer, R.W., Richards, D.A., Scott, E.M., Southon, J.R., Staff, R.A., Turney, C.S.M., Van der Plicht, J., 2013. Intcal13 and Marine13

radiocarbon age calibration curves 0-50,000 years cal BP. *Radiocarbon* 55 (4), 1869-1887.

Rodrigo-Gamiz, M., Martinez-Ruiz, F., Jiménez-Espejo, F.J., Gallego-Torres, D., Nieto-Moreno, V., Romero, O., Ariztegui, D., 2011. Impact of climate variability in the western Mediterranean during the last 20,000 years: oceanic and atmospheric responses. *Quat. Sci. Rev.* 30, 2018–2034.

Rodrigo-Gamiz, M., Martinez-Ruiz, F., Rodriguez-Tovar, F.J., Jimenez-Espejo, F.J., Pardo-Iguzquiza, E., 2014. Millennial- to centennial-scale climate periodicities and forcing mechanisms in the westernmost Mediterranean for the past 20,000 yr. *Quat. Res.* 81, 78–93.

Ruiz-Pérez, J.-M., Carmona, P., 2019. Turia river delta and coastal barrier-lagoon of Valencia (Mediterranean coast of Spain): Geomorphological processes and global climate fluctuations since Iberian-Roman times. *Quat. Sci. Rev.* 219, 84-101.

Sabatier, P., Dezileau, L., Condomines, M., Briqueu, L., Colin, C., Bouchette, F., Le Duff, M., Blanchemanche, P., 2008. Reconstruction of paleostorm events in a coastal lagoon (Hérault, South of France). *Mar. Geol.* 251, 224-232.

Sabatier, P., Dezileau, L., Colin, C., Briqueu, L., Bouchette, F., Martinez, P., Siani, G., Raynal, O., Von Grafenstein, U., 2012. 7000 years of paleostorm activity in the NW Mediterranean Sea in response to Holocene climate events. *Quat. Res.* 2012, 1-11.

Sadori, L., Giraudi, C., Masi, A., Magny, M., Ortu, E., Zanchetta, G., Izdebski, A., 2016. Climate, environment and society in southern Italy during the last 2000 years. A review of the environmental, historical and archaeological evidence. *Quat. Sci. Rev.* 136, 173-188.

Sanchez-Lopez, G., Hernandez, A., Pla-Rabes, S., Trigo, R.M., Toro, M., Granados, I., Saez, A., Masqué, P., Pueyo, J.J., Rubio-Inglés, M.J., Giralt, S., 2016. Climate reconstruction for

1236 the last two millennia in central Iberia: The role of East Atlantic (EA), North Atlantic
1237 Oscillation (NAO) and their interplay over the Iberian Peninsula. *Quat. Sci. Rev.* 149,
1238 135-150.
1239 Schofield, J.E., Edwards, K.J., Mighall, T.M., Martinez Cortizas, A., Rodriguez-Racedo, J.,
1240 Cook, G., 2010. An integrated geochemical and palynological study of human impacts,
1241 soil erosion and storminess from southern Greenland since c. AD 1000. *Palaeogeogr.*
1242 *Palaeoclimatol. Palaeoecol.* 295, 19-30.
1243 Serreze, M.C., Carse, F., Barry, R.G., Rogers, J.C., 1997. Icelandic Low cyclone activity:
1244 Climatological features, linkages with the NAO, and relationships with recent Changes
1245 in the Northern Hemisphere circulation. *J. Climate* 10, 453-464.
1246 Shabbar, A., Huang, J., Higuchi, K., 2001. The relationship between the wintertime North
1247 Atlantic oscillation and blocking episodes in the North Atlantic. *Int. J. Climatol.* 21,
1248 355-369.
1249 Shanahan, T.M., Overpeck, J.T., Anchukaitis, K.J., Beck, J.W., Cole, J.E., Dettman, D.L., Peck,
1250 J.A., Scholz, C.A., King, J.W., 2009. Atlantic forcing of persistent drought in West Africa.
1251 *Science* 324, 377-380.
1252 Siani, G., Paterne, M., Arnold, M., Bard, E., Métivier, B., Tisnerat, N., Bassinot, F., 2000.
1253 Radiocarbon reservoir ages in the Mediterranean Sea and Black Sea. *Radiocarbon* 42
1254 (2), 271-280.
1255 Sicre, M.-A., Jalali, B., Martrat, B., Schmidt, S., Bassetti, M.-A., Kallel, N., 2016. Sea surface
1256 temperature variability in the North Western Mediterranean Sea (Gulf of Lion) during
1257 the Common Era. *Earth Planet. Sci. Lett.* 456, 124-133.
1258 Simms, A.R., Rodriguez, A.B., 2015. The influence of valley morphology on the rate of
1259 bayhead delta progradation. *J. Sediment. Res.* 85, 38-44.

1260 Simms, A.R., Rodriguez, A.B., Anderson, J.B., 2018. Bayhead deltas and shorelines:
1261 Insights from modern and ancient examples. *Sediment. Geol.* 374, 17-35.
1262 Somoza, L., Barnolas, A., Arasa, A., Maestro, A., Rees, J.G., Hernandez-Molina, F.J., 1997.
1263 Architectural stacking patterns of the Ebro delta controlled by Holocene high-
1264 frequency eustatic fluctuations, delta-lobe switching and subsidence processes.
1265 *Sediment. Geol.* 117, 11-32.
1266 Sorrel, P., Tessier, B., Demory, F., Delsinne, N., Mouazé, D., 2009. Evidence for millennial-
1267 scale climatic events in the sedimentary infilling of a macrotidal estuarine system, the
1268 Seine estuary (NW France). *Quat. Sci. Rev.* 28, 499-516.
1269 Spada, G., Stocchi, P., 2007. SELEN: A Fortran 90 program for solving the "sea-level
1270 equation". *Comput. Geosci.* 33, 538-562.
1271 Stanley, J.-D., 2001. Dating modern deltas: progress, problems, and prognostics. *Annu.*
1272 *Rev. Earth Planet. Sci.* 29, 257-294.
1273 Stanley, J.-D., Warne, A.G., 1994. Worldwide initiation of Holocene marine deltas by
1274 deceleration of sea-level rise. *Science* 265 (5169), 228-231.
1275 Stanley, J.-D., Hait, A.K., 2000. Deltas, radiocarbon dating, and measurements of sediment
1276 storage and subsidence. *Geology* 28 (4), 295-298.
1277 Striewski, B., Mayr, C., Flenley, J., Naumann, R., Turner, G., Lücke, A., 2009. Multi-proxy
1278 evidence of late Holocene human-induced environmental changes at Lake Pupuke,
1279 Auckland (New Zealand). *Quat. Int.* 202, 69-93.
1280 Stuiver, M., Reimer, P.J., Reimer, R.W., 2019. CALIB 7.1 [WWW program] at
1281 http://calib.org
1282 Toonen, W.H.J., Kleinhans, M.G., Cohen, K.M., 2012. Sedimentary architecture of
1283 abandoned channel fills. *Earth Surf. Proc. Land.* 37, 459-472.

1284 Toutin-Morin, N., Bonijoly, D., Brocard, C., Broutin, J., Crévola, G., Dardeau, G., Dubar, M.,
1285 Féraud, J., Giraud, J.D., Godefroy, P., Laville, P., Meinesz, A., 1994. *Notice explicative,*
1286 *Carte géologique de la France (1/50000), feuille Fréjus-Cannes (1024)*. BRGM Editions,
1287 Orléans, 187 p.
1288 Trigo, I.F., Bigg, G.R., Davies, T.D., 2002. Climatology of cyclogenesis mechanisms in the
1289 Mediterranean. *Mon. Weather Rev.* 130, 549-569.
1290 Trigo, R.M., Trigo, I.F., DaCamara, C.C., Osborn, T.J., 2004. Climate impact of the European
1291 winter blocking episodes from the NCEP/NCAR Reanalyses. *Clim. Dynam.* 23, 17-28.
1292 Trouet, V., Esper, J., Graham, N.E., Baker, A., Scourse, J.D., Frank, D.C., 2009. Persistent
1293 positive North Atlantic Oscillation mode dominated the Medieval Climate Anomaly.
1294 *Science* 324, 78-80.
1295 Trouet, V., Scourse, J.D., Raible, C.C., 2012. North Atlantic storminess and Atlantic
1296 Meridional Overturning Circulation during the last Millennium: Reconciling
1297 contradictory proxy records of NAO variability. *Glob. Planet. Chang.* 84-85, 48-55.
1298 Vacchi, M., Marriner, N., Morhange, C., Spada, G., Fontana, A., Rovere, A., 2016. Multiproxy
1299 assessment of Holocene relative sea-level changes in the western Mediterranean: Sea-
1300 level variability and improvements in the definition of the isostatic signal. *Earth Sci.*
1301 *Rev.* 155, 172-197.
1302 Van der Plicht, J., 2004. Radiocarbon, the calibration curve and Scythian chronology. *In*
1303 Scott, E.M., Alekseev, A.Y., Zaitseva, G. (Eds.): *Impact of the environment on human*
1304 *migration in Eurasia*. Springer Netherlands, NATO Science Series, IV Earth and
1305 Environmental Sciences 42, 45-61.
1306 Véron, A., Morhange, C., Poirier, A., Angeletti, B., Bertoncello, F., 2018. Geochemical
1307 markers of human occupation in the lower Argens valley (Fréjus, France): from
1308 protohistory to Roman times. *J. Archaeol. Sci. Rep.* 17, 242-249.

Vis, G.-J., Bohncke, S.J.P., Schneider, H., Kasse, C., Coenraads-Nederveen, S., Zuurbier, K., Rozema, J., 2010. Holocene flooding history of the Lower Tagus Valley (Portugal). *J. Quat. Sci.* 25 (8), 1222-1238.

Wassenburg, J.A., Immenhauser, A., Richter, D.K., Niedermayr, A., Riechelmann, S., Fietzke, J., Scholz, D., Jochum, K.P., Fohlmeister, J., Schröder-Ritzrau, A., Sabaoui, A., Riechelmann, D.F.C., Schneider, L., Esper, J., 2013. Moroccan speleothem and tree ring records suggest a variable positive state of the North Atlantic Oscillation during the Medieval Warm Period. *Earth Planet. Sci. Lett.* 375, 291-302.

Wilhelm, B., Arnaud, F., Sabatier, P., Crouzet, C., Brisset, E., Chaumillon, E., Disnar, J.-R., Guiter, F., Malet, E., Reyss, J.-L., Tachikawa, K., Bard, E., Delannoy, J.-J., 2012. 1400 years of extreme precipitation patterns over the Mediterranean French Alps and possible forcing mechanisms. *Quat. Res.* 78, 1-12.

Wirth, S.B., Glur, L., Gilli, A., Anselmetti, F.S., 2013. Holocene flood frequency across the Central Alps – solar forcing and evidence for variations in North Atlantic atmospheric circulation. *Quat. Sci. Rev.* 80, 112-128.

Legend of tables and figures

Table 1. Radiocarbon dates from the Argens River delta system. Elevation in reference to LiDAR data (Litto3D, IGN/SHOM). LPT1: La Plaine T1, LPT3: La Plaine T3, TAT2: Théâtre d'agglomération T2. *: age inversion.

Table 2. Nominal relative sea level (RSL) with minimum and maximum errors from Vacchi et al. (2016). The RSL prediction was computed using the open source code SELEN (Spada and Stocchi, 2007) that employs the ICE-5G (VM2) model from Peltier (2004).

Fig. 1. Location of the Argens River in the northwestern Mediterranean (A) and topographic and geological setting of the Argens River delta system (B). Coordinate system: WGS 1984 World Mercator (A) and RGF 1993 Lambert-93 (B). ITCZ: intertropical convergence zone. 1, 2: Durance River sites (Arnaud-Fassetta et al., 2010; Benito et al., 2015a). Marine records of terrigenous material in sediments from the western Mediterranean basin: KSGC-31 site (Jalali et al., 2016); MD99-2343 site (Frigola et al., 2007); 305G, 306G, 384B and 436B sites (NietoMoreno et al., 2011, 2013a, 2013b); DP30 site (Goudeau et al., 2014, 2015). References of published cores and archaeological surveys: Dubar (2004) for Verteil core, Allinne et al. (2006) for ESC1 core, Devillers and Bonnet (2006) for VIL2 core, Excoffon et al. (2006) and Devillers et al. (2007) for Théâtre d'agglomération T2 archaeological survey, Excoffon et al. (2010) for Villa

Romana archaeological survey, Bony et al. (2011) for FIX, FXI and SC6 cores, Bertoncello et al. (2014a) for PL1 and PAL1 cores, Bertoncello et al. (2016) for La Plaine T1-T3 archaeological survey.

Fig. 2. Stratigraphy, magnetic susceptibility, geochemistry and malacofauna of BN1 core in the Argens River delta system. Vertical dashed lines correspond to the mean values of variables.

Fig. 3. Stratigraphy, magnetic susceptibility, geochemistry and malacofauna of BN5 core in the Argens River delta system. Vertical dashed lines correspond to the mean values of variables.

Fig. 4. Malacological diagram of BN1 core. Main environmental conditions inferred from a cluster analysis by constrained incremental sum of squares (CONISS) with a dissimilarity coefficient corresponding to Edwards and Cavalli-Sforza's chord distance (Grimm, 1987).

Fig. 5. Malacological diagram of BN5 core. Main environmental conditions inferred from a cluster analysis by constrained incremental sum of squares (CONISS) with a dissimilarity coefficient corresponding to Edwards and Cavalli-Sforza's chord distance (Grimm, 1987).

Fig. 6. 2D age-elevation models in the coastal plain of the Argens River delta system. The data used in the age-elevation models correspond to the median probability of calibrated ages (white dot) from the compilation of radiocarbon ages available in the Argens River delta system (Table 1) and to modern elevation based on LiDAR data (Litto3D, IGN/SHOM) for the year 2015 (blue triangle). Numbers in brackets represent the 2-σ uncertainty interval of calibrated ages (Table 1). The radiocarbon ages in red were discarded to avoid age reversals (see explanation in text). References for radiocarbon ages, lithology and depositional environment (if available): Dubar (2004) for Verteil core, Allinne et al. (2006) for ESC1 core, Devillers and Bonnet (2006) for VIL2 core, Devillers et al. (2007) for Théâtre d'agglomération T2 archaeological survey, Excoffon et al. (2010) for Villa Romana archaeological survey, Bertoncello et al. (2014a) for PL1 and PAL1 cores, Bertoncello et al. (2016) for La Plaine T1 and T3 archaeological surveys, and this study for BN1 and BN5 cores. The data point for Villa Romana was estimated from the reconstruction of the shoreline around 2000 cal yr BP based on archaeological data, radiocarbon ages and relative sea level reconstruction (Excoffon et al., 2010; Vacchi et al., 2016). Location of age-elevation models A1-3 in Fig. 1B. Models interpolated with a thin plate spline kernel function and an 8-sector neighbourhood search algorithm. The isochrones of the unconfined bayhead delta were obtained by shifting the LiDAR data along the BN5 age-elevation model. (For interpretation of the references to colour in this figure legend, the reader is referred to the web version of this article.)

Fig. 7. Interpolated maps of sediment thickness in the Argens River delta system over the past 2500 years. LPT1 and LPT3: La Plaine T1 and T3 archaeological surveys, TAT2: Théâtre d'agglomération T2 archaeological survey, VR: Villa Romana archaeological survey. Models interpolated with a multiquadratic kernel function and an 8-sector neighbourhood search algorithm.

Fig. 8. Palaeoelevation in the Argens River delta system over the past 2500 years. LPT1 and LPT3: La Plaine T1 and T3 archaeological surveys, TAT2: Théâtre d'agglomération T2 archaeological survey, VR: Villa Romana archaeological survey. The past sea levels used in the elevation models are based on the relative sea level (RSL) in the western Ligurian Sea determined by the ICE-5G (VM2) geophysical model (Peltier, 2004) for the last 2500 years (Table 2). In this area, a good fit between the model and available geological sea level proxies was observed along the whole Holocene (Vacchi et al., 2016). The reconstructed RSL at 2000 cal yr BP is consistent with the Roman sea level deduced from marine encrustation found on archaeological harbour structures, a very robust methodology to infer the RSL position in the Mediterranean Sea (Morhange and Marriner, 2015; Vacchi et al., 2016). The RSL in the *Forum Iulii* harbour (Fig. 1B) was estimated at -40 ± 10 cm (Morhange et al., 2013) or -33 ± 6 cm (Devillers et al., 2007) between the first century BCE and the first century CE.

Fig. 9. Evolution of sediment flux and fluvial activity in the Argens River delta system (ARDS) and comparison with riverine flooding frequency in the southern French Alps over the past 2500 years. (a) Sediment fluxes calculated for each 500-year interval by

1426 estimating the volume of sediment using the ArcGIS 10 Surface Volume tool with either
1427 (1) the elevation models in Fig. 8 and reference planes corresponding to the mean
1428 relative sea level from Vacchi et al. (2016) for each 500-year interval for the confined
1429 bayhead delta, or (2) the LiDAR data shifted along the BN5 age-elevation model (Fig. 6,
1430 age profile A1) and a reference plane at 20 m below present sea level for the unconfined
1431 bayhead delta. (b) Proxy records of riverine input and fluvial activity corresponding to
1432 the average of the standard scores of Si/Al, K/Al and Rb/Al ratios from BN1 core with an
1433 age scale established by using AnalySeries 2.0 (Paillard et al., 1996). (c) Proxy records of
1434 riverine input and fluvial activity corresponding to the average of the standard scores of
1435 Si/Al, K/Al and Rb/Al ratios from BN5 core with an age scale established by using
1436 AnalySeries 2.0 (Paillard et al., 1996). (d) Periods of relatively high flood frequency of
1437 the lower Durance River and its tributaries (site 1 in Fig. 1A) in the southern French
1438 Alps (Arnaud-Fassetta et al., 2010; Benito et al., 2015a). (e) Periods of relatively high
1439 flood frequency of the middle Durance River and its tributaries (site 2 in Fig. 1A) in the
1440 southern French Alps (Arnaud-Fassetta et al., 2010; Benito et al., 2015a). (f) Relative
1441 cumulative probability density function of radiocarbon dates from flood and extreme
1442 fluvial event units of rivers in southeastern France (Fig. 1A) (Benito et al., 2015a). IACP:
1443 Iron Age Cold Period, RWP: Roman Warm Period, DACP: Dark Ages Cold Period, MWP:
1444 Medieval Warm Period, LIA: Little Ice Age, GW: Global Warming.
1445
1446
1447 Fig. 10. Comparison of sediment flux and fluvial activity in the Argens River delta system
1448 (ARDS) with geomorphic factors and climate proxy records over the last 2500 years. (a)
1449 Mean slope of the ARDS longitudinal gradient between Verteil and BN5 from age profiles
1450 in Fig. 6. (b) Volume of accommodation space of the ARDS estimated using the ArcGIS 10

Surface Volume tool with the elevation models in Fig. 8 and reference planes corresponding to the relative sea level from Vacchi et al. (2016). (c) Subaqueous sediment flux in the ARDS with an error range of ± 20%. (d) Subaerial sediment flux in the ARDS with an error range of ± 20%. (e) Fluvial activity in the easternmost part of the lower Argens valley corresponding to the average of the standard scores of fluvial activity at BN1 and BN5 (Fig. 9b-c) resampled at a 5-years interval by linear interpolation using AnalySeries 2.0 (Paillard et al., 1996), along with period of autogenic control (see section 7.2). (f) Mean band width of three radiometrically dated speleothems from the Uamh an Tartair cave in northwestern Scotland (Fig. 1A) (Proctor et al., 2002). (g) Potential leading mode of atmospheric circulation in Europe (see section 7.3). (h) Alkenone-based sea surface temperature (SST) in the northwestern Mediterranean with cold relapse episodes (CR4-6) from the KSCG-31 core in the Gulf of Lions (Fig. 1A) (Jalali et al., 2016). (i) Storm activity in southeastern France from the sedimentary record of the Bagnas lagoon (Fig. 1A) (Degeai et al., 2015). (j) Storm activity in southeastern France from the sedimentary record of the Pierre Blanche lagoon (Fig. 1A) (Sabatier et al., 2012). (k) Storm activity from sedimentary records in the Seine River estuary in northwestern France (Fig. 1A) (Sorrel et al., 2009). (l) Potential second or third mode of atmospheric circulation in Europe (see section 7.3). (m) 5-yr averaged oxygen isotope record of authigenic carbonate from Lake Bosumtwi in Ghana (Fig. 1A) (Shanahan et al., 2009). NAO: North Atlantic oscillation, EA: East Atlantic pattern, EA/WR: East Atlantic/West Russian pattern, IACP: Iron Age Cold Period, RWP: Roman Warm Period, DACP: Dark Ages Cold Period, MWP: Medieval Warm Period, LIA: Little Ice Age, GW: Global Warming.

Fig. 11. Late Holocene atmospheric circulation patterns and climatic conditions in the North Atlantic and Europe during the periods of high fluvial activity driven by climate change in the Argens lower valley. Empirical orthogonal functions (EOF1-3) calculated from sea level pressure reconstructed by Luterbacher et al. (2002) for the period 1500-1999 CE. 1: Argens River delta system, 2: Gulf of Lions, 3: Bagnas and Pierre Blanche lagoons, 4: Seine River estuary, SST: sea surface temperature, NAO: North Atlantic oscillation, EA: East Atlantic pattern, EA/WR: East Atlantic/West Russian pattern, ITCZ: intertropical convergence zone, IACP: Iron Age Cold Period, RWP: Roman Warm Period, DACP: Dark Ages Cold Period, LIA: Little Ice Age.

1486 Table 1
1487

Core or trench	Elevation (m)	Laboratory code	Material	^{14}C age (BP)	Reference	2-σ interval of calibrated age (cal yr BP)	Median probability of calibrated age (cal yr BP)
BN1	0.30	Poz-81546	Charcoal	375 ± 30	This study	504-318	442
BN1	-3.60	Poz-81547	Charcoal	2520 ± 30	This study	2744-2492	2595*
BN1	-5.60	Poz-81608	Charcoal	2215 ± 30	This study	2322-2151	2231*
BN1	-7.00	Poz-81548	Charcoal	3330 ± 35	This study	3678-3467	3565*
BN1	-8.60	Poz-81549	Charcoal	2085 ± 30	This study	2143-1990	2058
BN1	-10.10	Poz-81550	Charcoal	2480 ± 30	This study	2723-2385	2585
BN5	-7.86	Lyon-13936	Wood	2055 ± 30	This study	2118-1934	2023*
BN5	-9.98	Lyon-13937	Wood	1975 ± 30	This study	1993-1871	1925
BN5	-12.33	Lyon-13938	Wood	2175 ± 30	This study	2310-2072	2231
BN5	-13.67	Lyon-13939	Wood	2195 ± 30	This study	2313-2133	2237
ESC1	0.18	Poz-12168	Seed	680 ± 30	Allinne et al. (2006)	680-561	652
ESC1	-1.57	Poz-12167	Seed	2535 ± 30	Allinne et al. (2006)	2747-2495	2625
ESC1	-2.52	Poz-12166	Seed	3735 ± 35	Allinne et al. (2006)	4227-3980	4089*
ESC1	-4.82	Poz-9593	Charcoal	3535 ± 35	Allinne et al. (2006)	3904-3702	3816
LPT1	3.44	Poz-78590	Charcoal	155 ± 30	Bertoncello et al. (2016)	284-0	174
LPT1	3.14	Poz-78591	Charcoal	175 ± 30	Bertoncello et al. (2016)	293-0	180
LPT1	2.44	Poz-78589	Charcoal	1315 ± 30	Bertoncello et al. (2016)	1295-1183	1259
LPT3	3.05	Poz-78593	Charcoal	4125 ± 30	Bertoncello et al. (2016)	4817-4531	4667*
LPT3	2.45	Poz-80846	Charcoal	960 ± 50	Bertoncello et al. (2016)	960-764	859
PAL1	-0.74	Lyon-5430	Seed	1075 ± 35	Bertoncello et al. (2014a)	1057-930	982
PAL1	-1.84	Lyon-5431	Seed	1285 ± 35	Bertoncello et al. (2014a)	1294-1097	1232*

PAL1	-2.34	Lyon-5432	Seed	1285 ± 35	Bertoncello et al. (2014a)	1294-1097	1232
PAL1	-8.84	Lyon-5061	Seed	2145 ± 30	Bertoncello et al. (2014a)	2304-2009	2137
PAL1	-14.34	Lyon-5062	Seed	2210 ± 30	Bertoncello et al. (2014a)	2320-2149	2232
PAL1	-17.34	Lyon-5433	Seed	2800 ± 40	Bertoncello et al. (2014a)	2998-2791	2904
PL1	1.49	Lyon-4223	Charcoal	1540 ± 35	Bertoncello et al. (2014a)	1525-1356	1448
PL1	-1.21	Lyon-4221	Seed	2515 ± 40	Bertoncello et al. (2014a)	2746-2467	2593*
PL1	-1.76	Lyon-4228	Seed	2510 ± 30	Bertoncello et al. (2014a)	2740-2490	2590*
PL1	-3.41	Lyon-4226	Charcoal	3120 ± 35	Bertoncello et al. (2014a)	3442-3234	3340*
PL1	-3.56	Lyon-5434	Seed	2395 ± 35	Bertoncello et al. (2014a)	2687-2345	2425
PL1	-4.31	Lyon-4225	Charcoal	2450 ± 30	Bertoncello et al. (2014a)	2704-2361	2528
PL1	-6.76	Lyon-4224	Seed	2490 ± 40	Bertoncello et al. (2014a)	2738-2381	2583
PL1	-7.51	Lyon-5435	Charcoal	4200 ± 45	Bertoncello et al. (2014a)	4851-4584	4730*
PL1	-8.81	Lyon-4222	Charcoal	2820 ± 35	Bertoncello et al. (2014a)	3057-2846	2924*
PL1	-10.06	Lyon-4219	Charcoal	2610 ± 40	Bertoncello et al. (2014a)	2843-2540	2749
TAT2	-0.33	Poz-14372	Marine shell	2345 ± 30	Devillers et al. (2007)	2087-1888	1983
Verteil	-2.41	Ly 5889	Peat	3050 ± 75	Dubar et al. (2004)	3443-3008	3247
VIL2	-2.25	Poz-10916	Charcoal	915 ± 30	Devillers and Bonnet (2006)	920-762	848
VIL2	-2.90	Poz-10917	Charcoal	1340 ± 30	Devillers and Bonnet (2006)	1305-1185	1280
VIL2	-5.65	Poz-10918	Charcoal	2325 ± 30	Devillers and Bonnet (2006)	2426-2208	2345
VIL2	-7.75	Poz-10922	Marine shell	5190 ± 30	Devillers and Bonnet (2006)	5634-5478	5571

1490 Table 2
1491

Age (cal yr BP)	Minimum RSL (m)	Nominal RSL (m)	Maximum RSL (m)
0	0.00	0.00	0.00
500	-0.14	-0.07	0.06
1000	-0.28	-0.13	0.12
1500	-0.43	-0.20	0.19
2000	-0.58	-0.28	0.26
2500	-0.78	-0.38	0.32

1492
1493
1494

1495 Figure 1 (two-column)

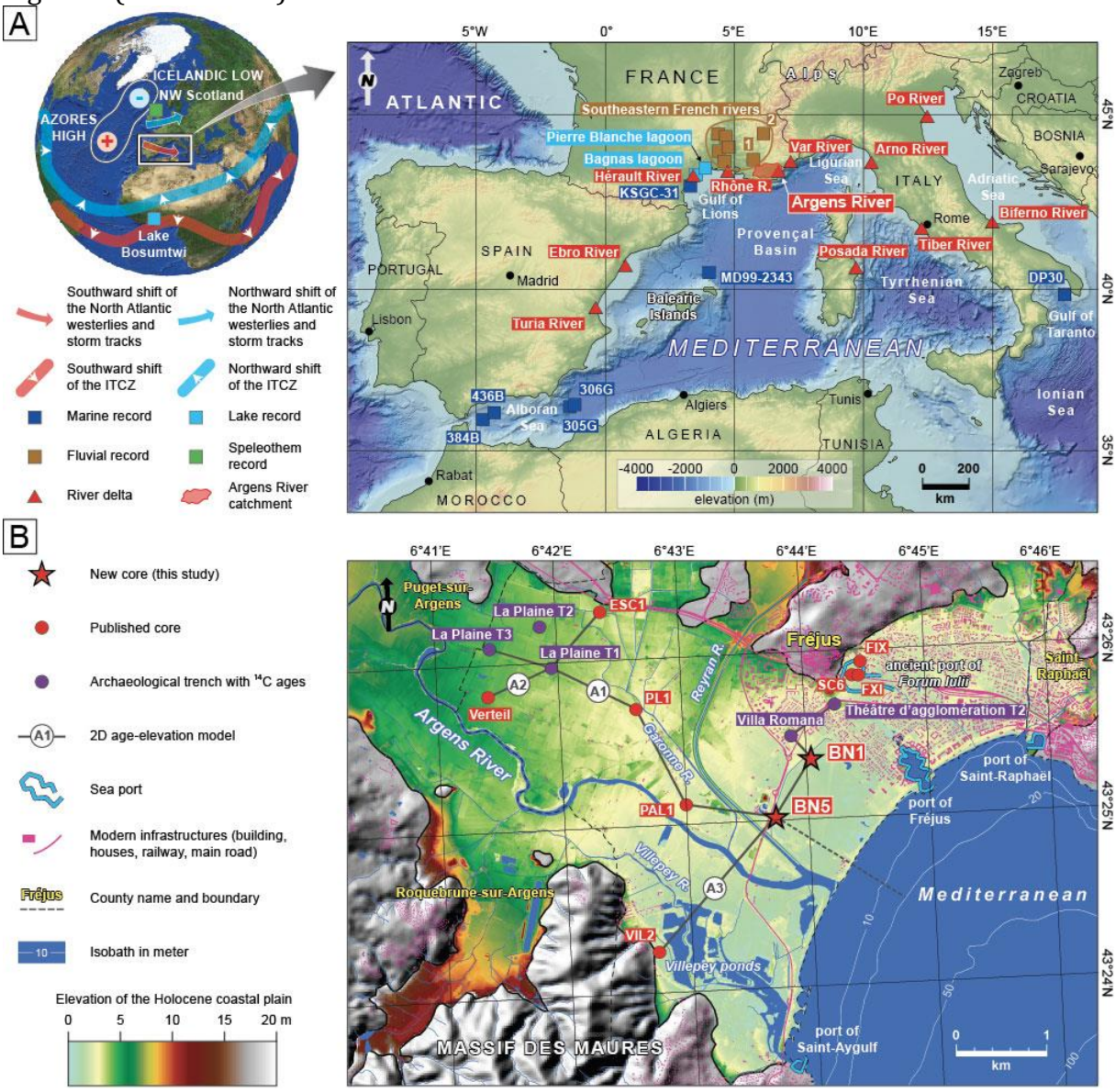

1496

1497 Figure 2 (two-column)

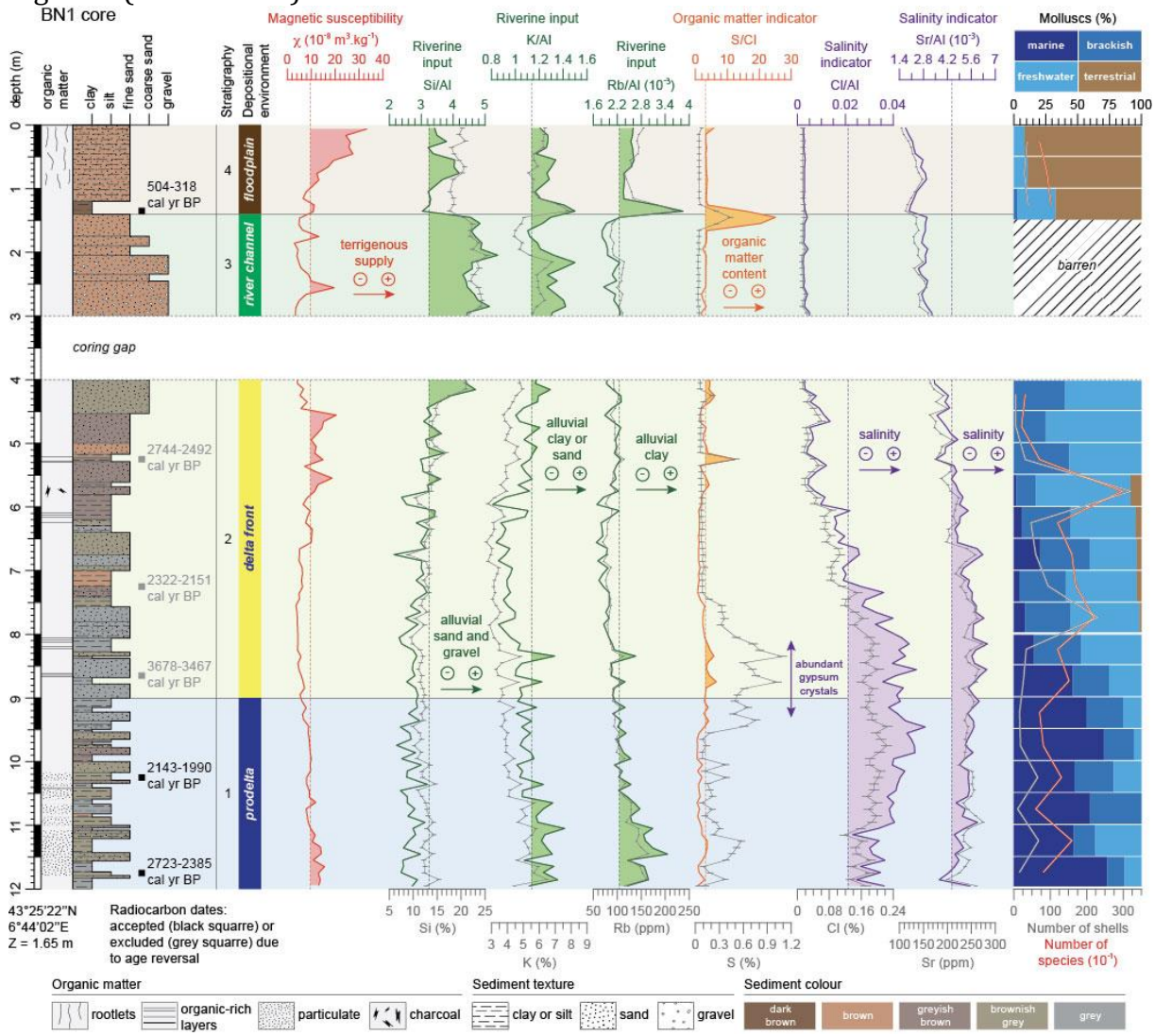

1498

1499 Figure 3 (two-column)

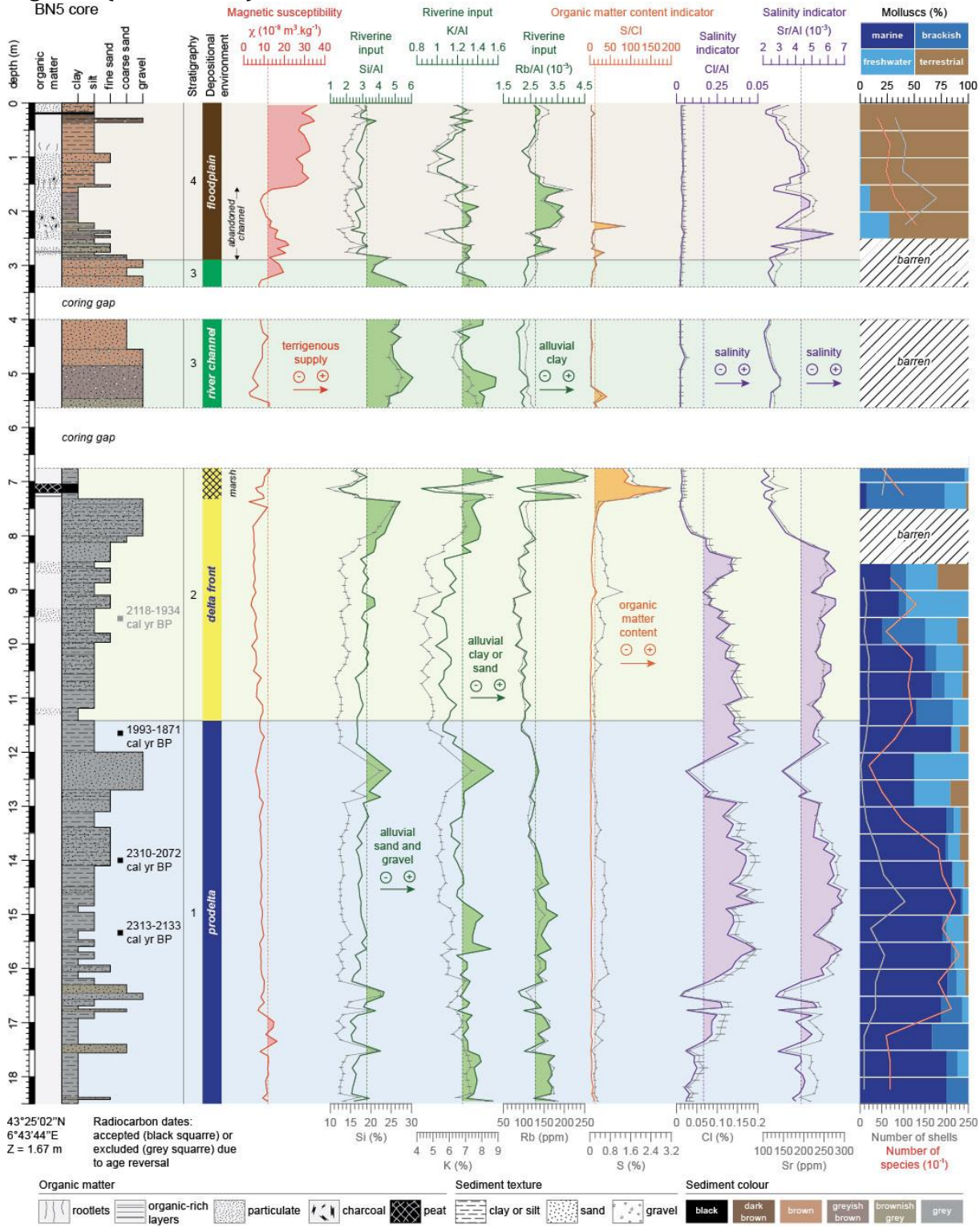

1500

Figure 4 (two-column)

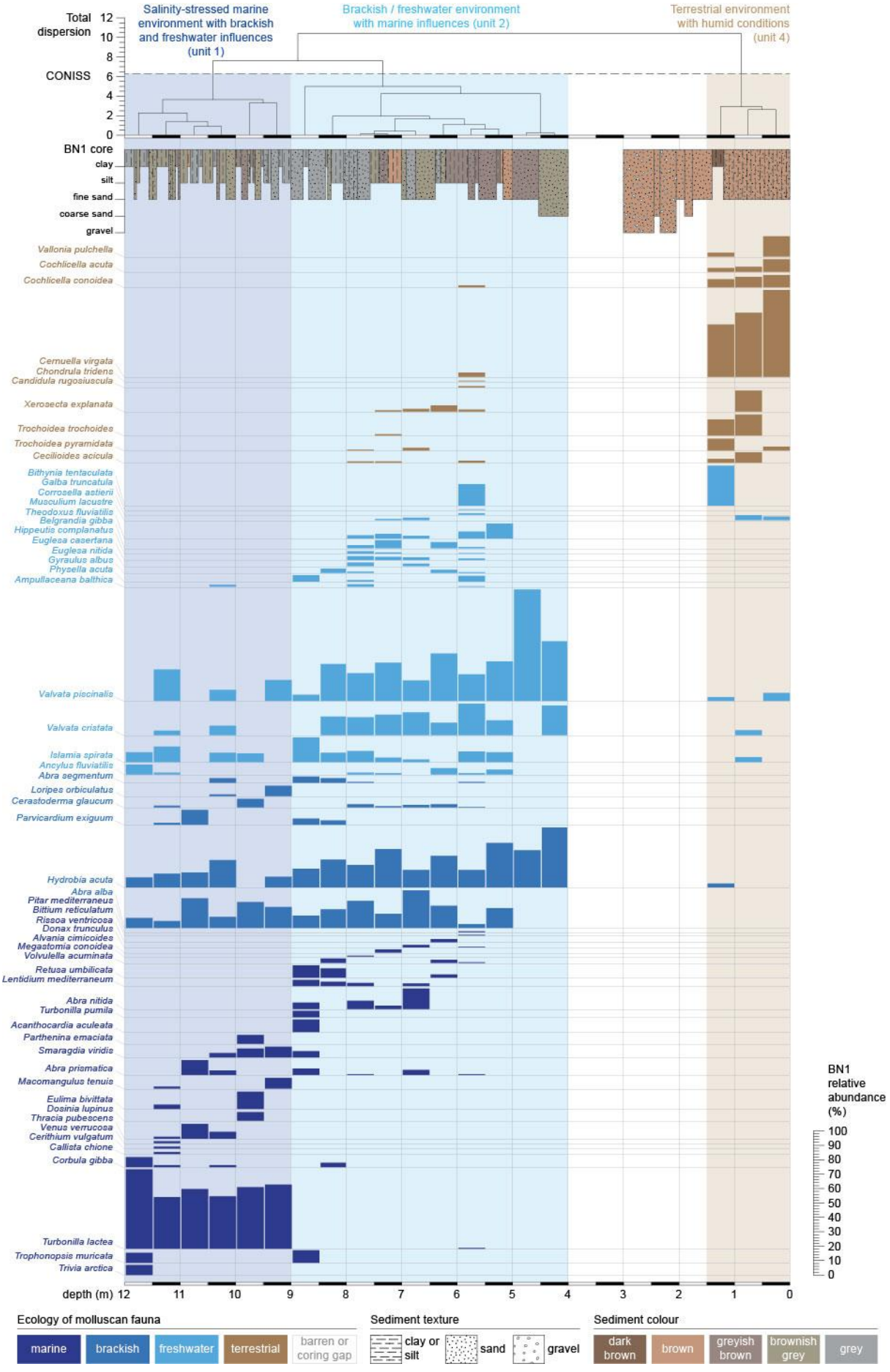
Salinity-stressed marine environment with brackish and freshwater influences (unit 1)
Brackish / freshwater environment with marine influences (unit 2)
Terrestrial environment with humid conditions (unit 4)
Total dispersion
CONISS
BN1 core
clay
silt
fine sand
coarse sand
gravel
Vallonia pulchella
Cochlicella acuta
Cochlicella conoidea
Cernuella virgata
Chondrula tridens
Candidula rugosiuscula
Xerosecta explanata
Trochoidea trochoides
Trochoidea pyramidata
Cecilioides acicula
Bithynia tentaculata
Galba truncatula
Corrosella astieri
Musculium lacustre
Theodoxus fluviatilis
Belgrandia gibba
Hippeutis complanatus
Euglesa casertana
Euglesa nitida
Gyraulus albus
Physella acuta
Ampullaceana balthica
Valvata piscinalis
Valvata cristata
Islamia spirata
Ancylus fluviatilis
Abra segmentum
Loripes orbiculatus
Cerastoderma glaucum
Parvicardium exiguum
Hydrobia acuta
Abra alba
Pitar mediterraneus
Bittium reticulatum
Rissoa ventricosa
Donax trunculus
Alvania cimicoides
Megastomia conoidea
Volvulella acuminata
Retusa umbilicata
Lentidium mediterraneum
Abra nitida
Turbonilla pumila
Acanthocardia aculeata
Parthenina emaciata
Smaragdia viridis
Abra prismatica
Macomangulus tenuis
Eulima bivittata
Dosinia lupinus
Thracia pubescens
Venus verrucosa
Cerithium vulgatum
Calliata chione
Corbula gibba
Turbonilla lactea
Trophonopsis muricata
Trivia arctica
depth (m)
BN1 relative abundance (%)
Ecology of molluscan fauna
marine
brackish
freshwater
terrestrial
barren or coring gap
Sediment texture
clay or silt
sand
gravel
Sediment colour
dark brown
brown
greyish brown
brownish grey
grey

1503 Figure 5 (two-column)

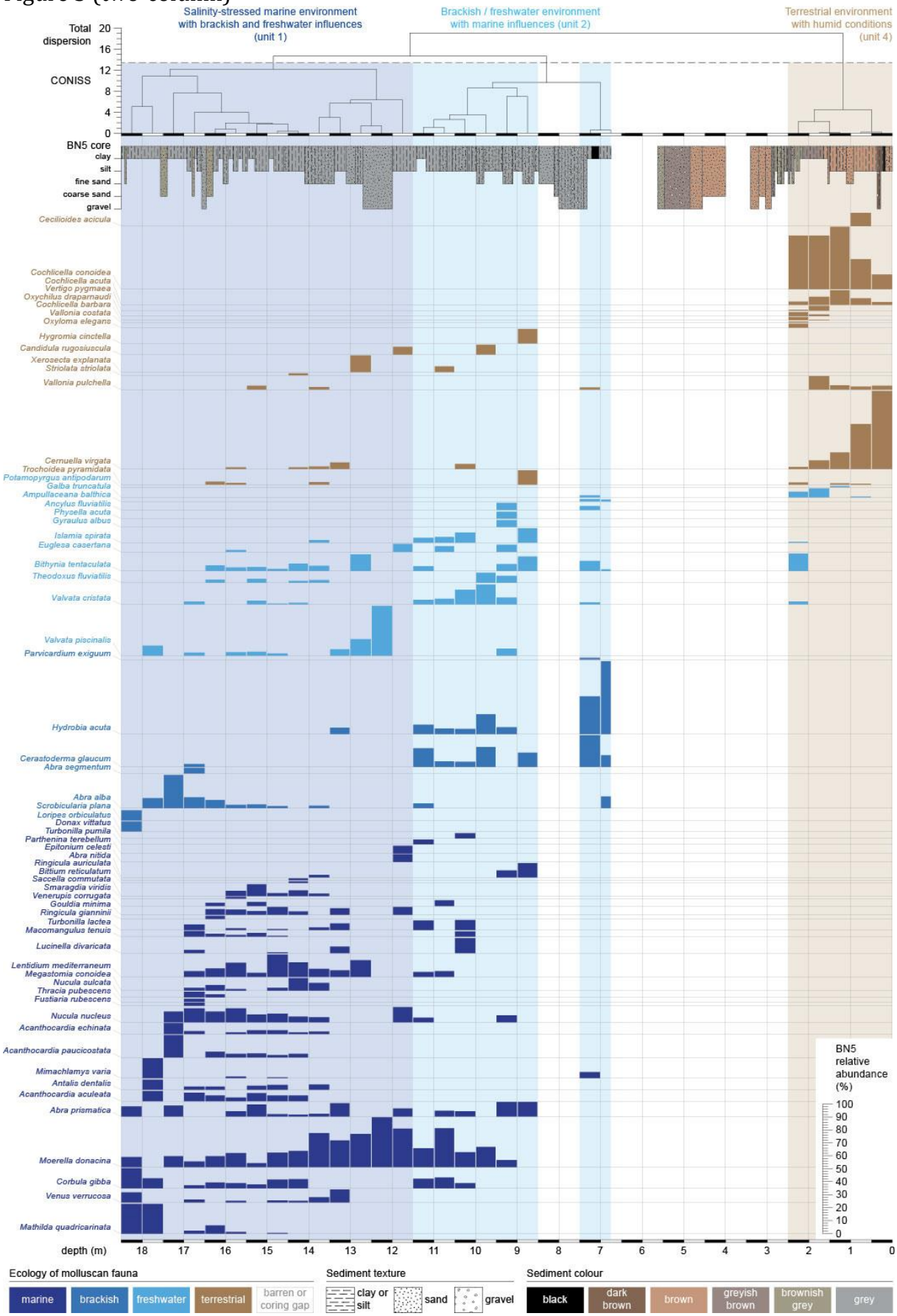

1504

1505 Figure 6 (two-column)

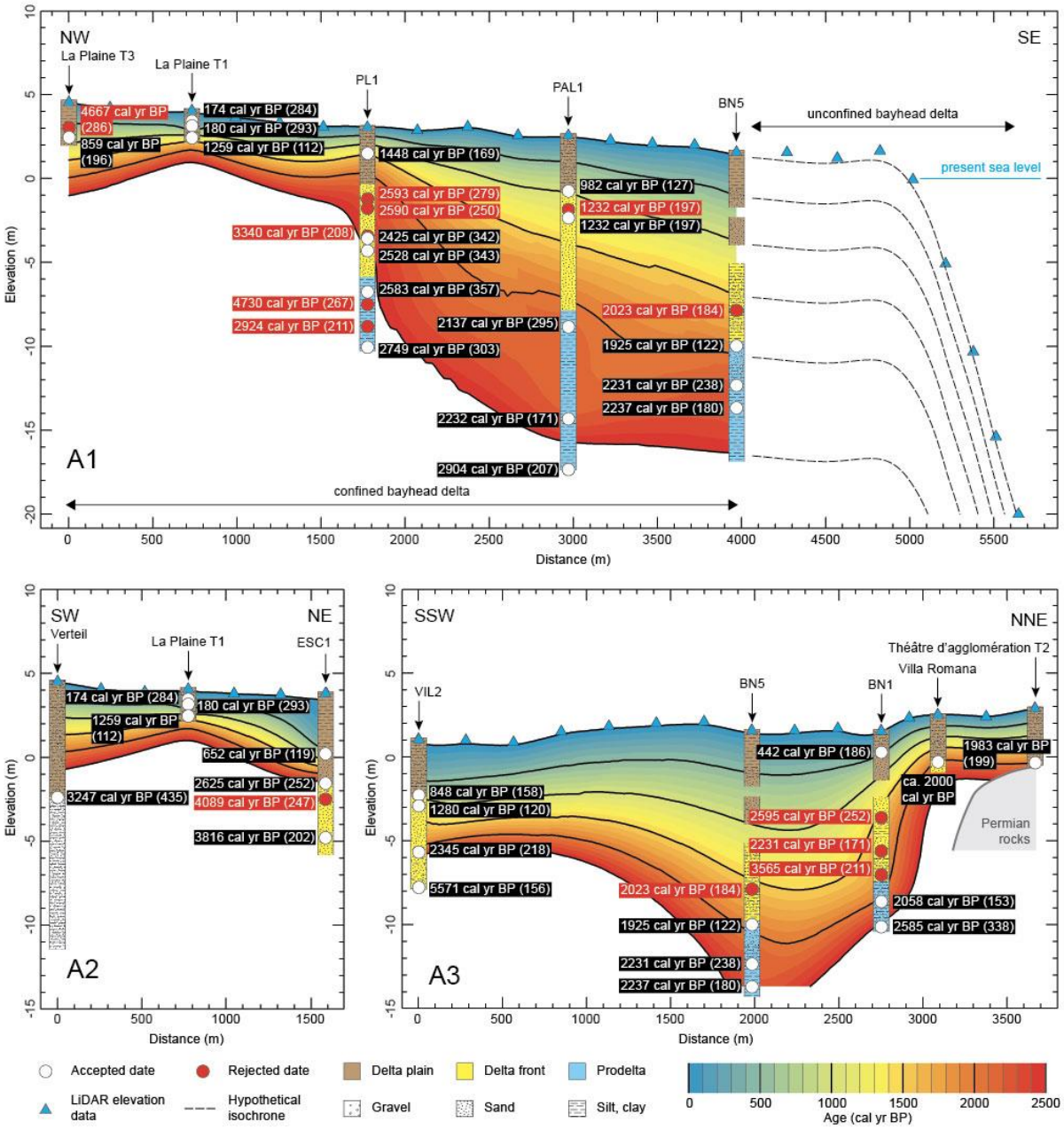

1506

1507 Figure 7 (two-column)

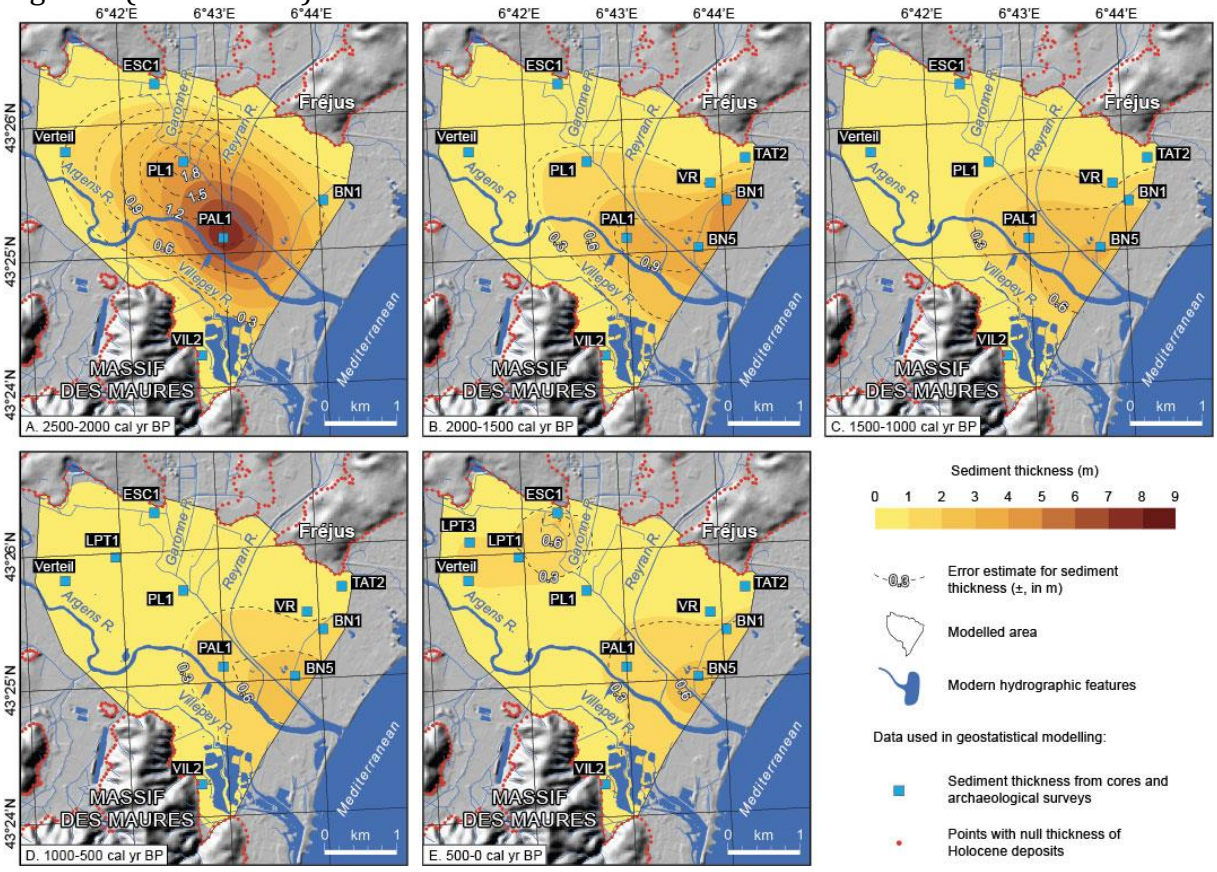

1508

1509 Figure 8 (two-column)

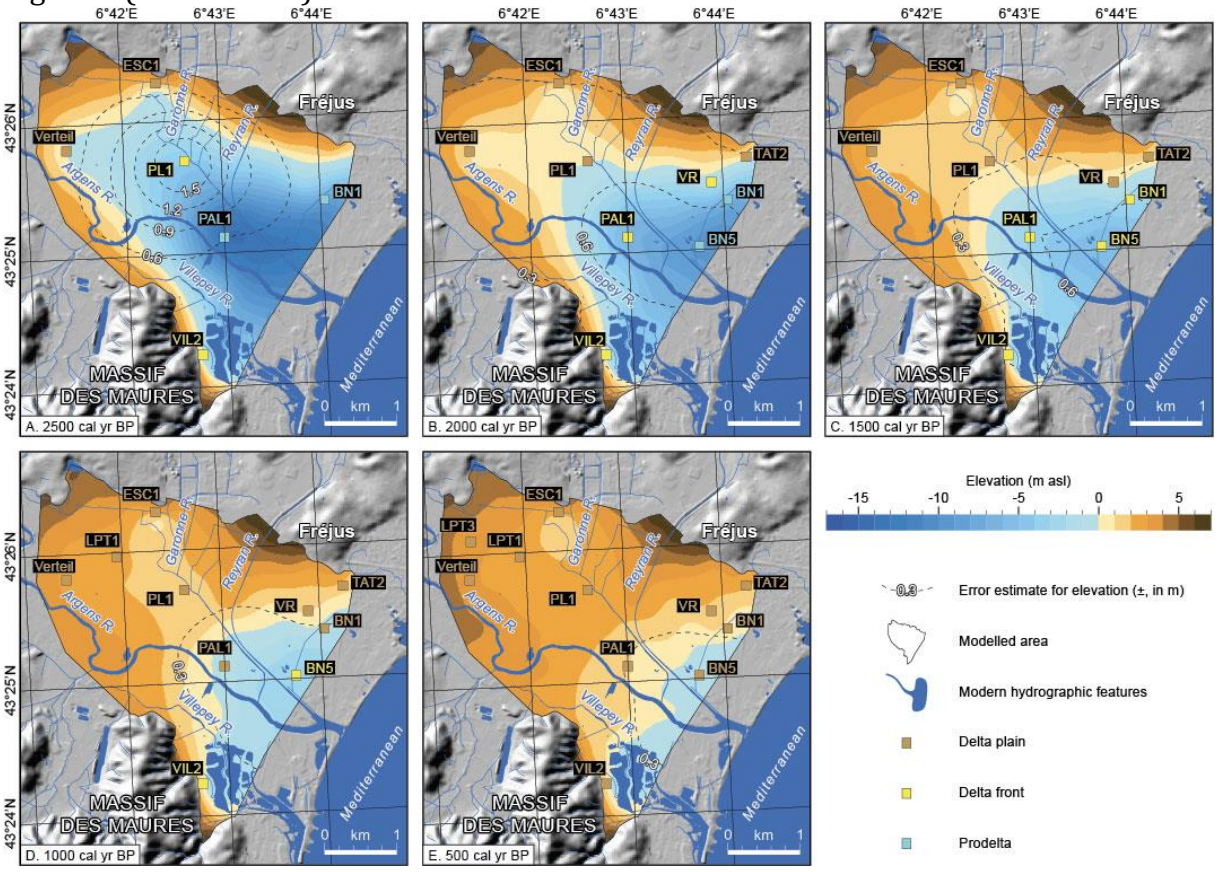

1510

1511 Figure 9 (single column)

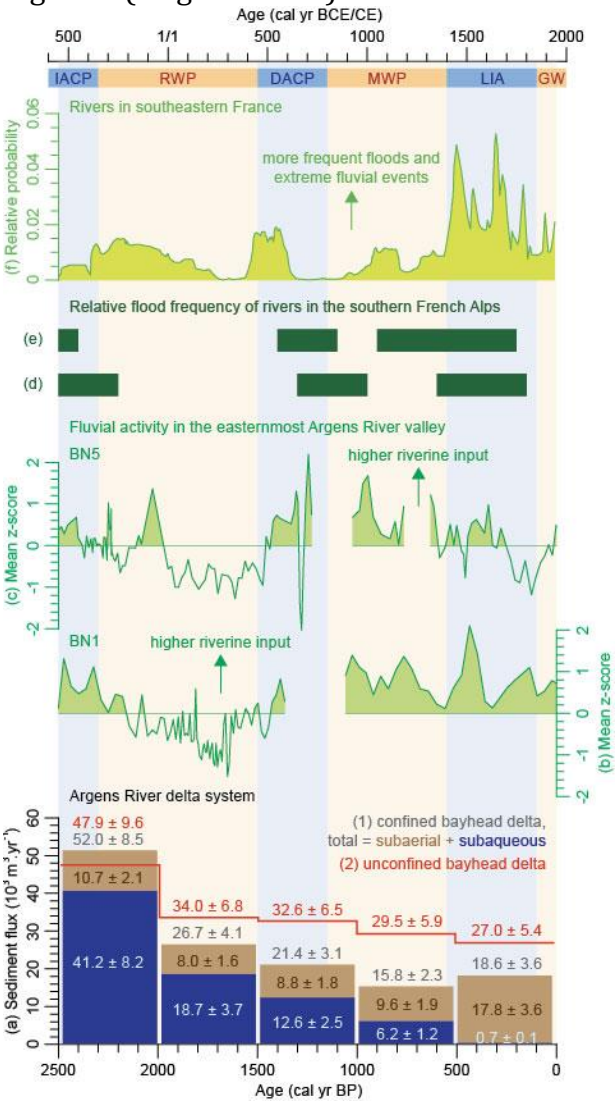

1512

1513 Figure 10 (single column)

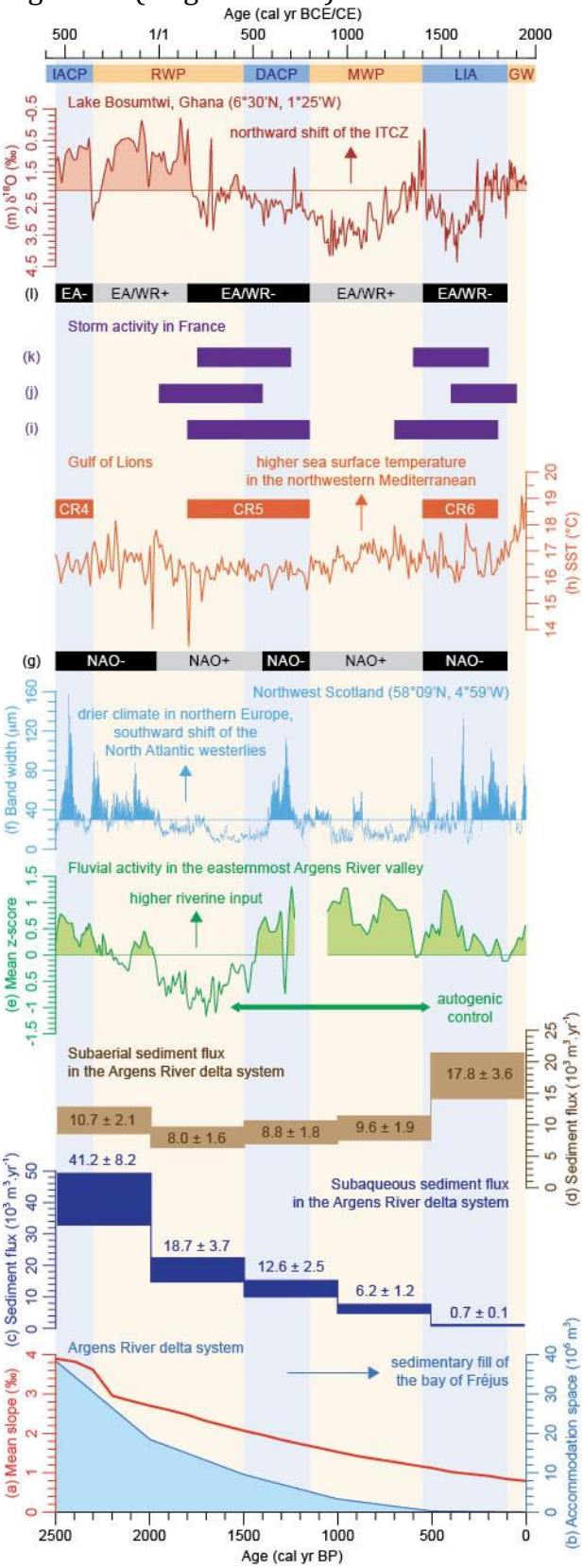

1514

1515 Figure 11 (single column)

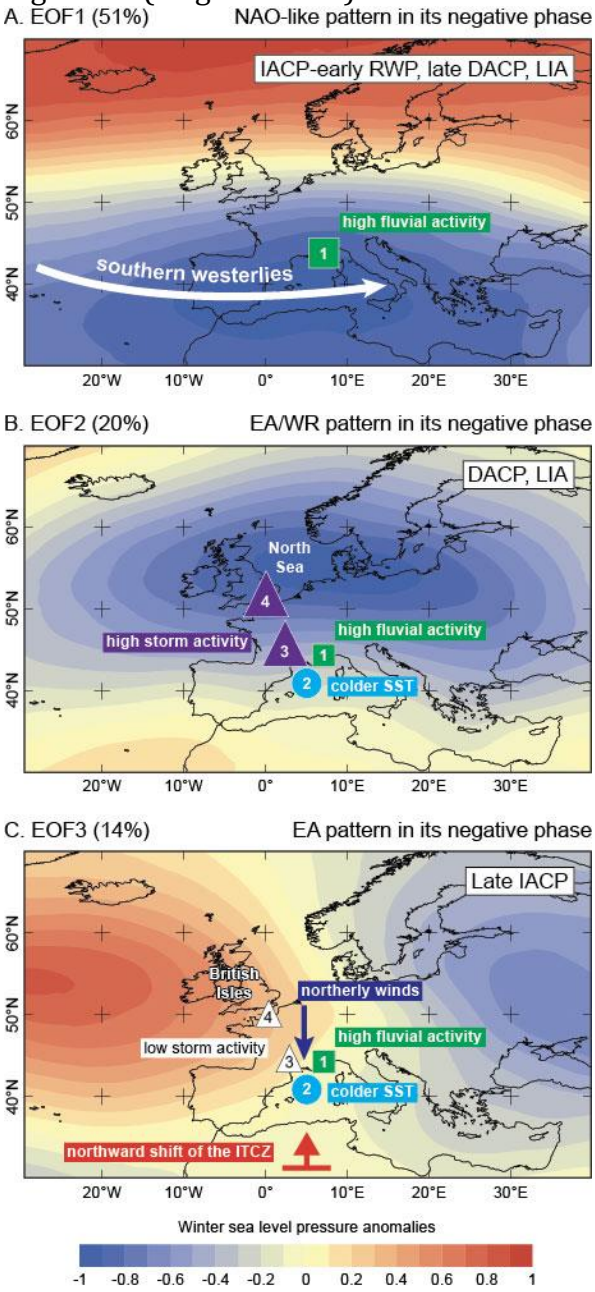

1516
1517